Corridors of crestal and radial faults linking salt diapirs in the Espírito Santo Basin, SE Brazil

Nathalia H. Mattos[1*] and Tiago M. Alves[1]

[1]3D Seismic Lab, School of Earth and Ocean Sciences, Cardiff University, Main Building-Park Place, CF10 3AT Cardiff, United Kingdom (mattosnh@cardiff.ac.uk)

Abstract

This work uses high-quality 3D seismic data to assess the geometry of fault families around salt diapir in SE Brazil (Espírito Santo Basin). It aims at evaluating the timings of fault growth, and suggests the generation of corridors for fluid migration linking discrete salt diapirs. Three salt diapirs, one salt ridge, and five fault families were identified based on their geometry and relative locations. Displacement-length (D-x) plots, Throw-depth (T-z) data and structural maps indicate that faults consist of multiple segments that were reactivated by dip-linkage following a preferential NE-SW direction. This style of reactivation and linkage is distinct from other sectors of the Espírito Santo Basin where the preferential mode of reactivation is by upwards vertical propagation. Reactivation of faults above a Mid-Eocene unconformity is also scarce in the study area. Conversely, two halokinetic episodes dated as Cretaceous and Paleogene are interpreted below a Mid-Eocene unconformity. This work is important as it recognises the juxtaposition of permeable strata across faults as marking the generation of fault corridors linking adjacent salt structures. In such a setting, fault modelling shows that fluid will migrate towards the shallower salt structures along the fault corridors first identified in this work.

Keywords: SE Brazil; Espírito Santo Basin; halokinesis; fault corridors; fluid flow.

1. Introduction

The investigation of subsurface faults and fractures is important in basin analysis as these structures play a crucial role in the entrapment and migration of fluids (Ainsworth, 2006; Bailey et al., 2002; Childs et al., 1997; Faulkner et al., 2010; Jolley et al., 2007; Knipe, 1997; Knipe et al., 1998; Walsh et al., 1998). Such a control of faults on fluid flow is particularly recorded in regions where the deposition of thick evaporite sequences is capable of influencing the structural styles of sedimentary basins (Brun and Fort, 2011; Hudec and Jackson, 2007; Smit et al., 2008; Stewart, 2006; Vendeville, 2002; Vendeville and Jackson, 1992). The movement of evaporite sequences through time (halokinesis) can result in the development of complex families of faults to form major structural compartments or, instead, promote the migration of fluids through reservoir and seal units (Alves et al., 2009; Carruthers et al., 2013; Fiduk et al., 2004; Gamboa et al., 2010; Jackson et al., 1994; Lohr et al., 2008; Stewart, 2006; Talbot et al., 1991). An early understanding of the mechanisms generating structural compartments in salt-rich basins can, therefore, increase the economic potential of new hydrocarbon prospects (Caine et al., 1996; Jolley et al., 2010, 2007; Knipe, 1997; Knipe et al., 1998).

The Espírito Santo Basin reveals a geological evolution that is similar to the Campos and Santos Basins, two of the most prolific hydrocarbon-bearing basins in SE Brazil (Bruhn et al., 2003; Chang et al., 1992; Cobbold et al., 2001; Demercian et al., 1993; Guardado et al., 2000; Guerra and Underhill, 2012; Meisling et al., 2001; Milani et al., 2001) (Fig. 1). Although being less known than its counterparts to the south, the Espírito Santo Basin hosts significant hydrocarbon accumulations in Cretaceous, Eocene-Oligocene and Miocene strata (Bruhn and Walker, 1997; Estrella et al., 1984; Fiduk et al., 2004; Katz and Mello, 2000). The Espírito Santo Basin also contains important volumes of evaporites, similarly to sedimentary basins in the Gulf of Mexico (Diegel et al., 1995; Rowan et al., 1999; Talbot, 1993), West Africa (Duval et al., 1992; Hudec and Jackson, 2002; Morley and Guerin, 1996) and Norway (Chand et al., 2008; Henriksen et al., 2011; Kane et al., 2010; Koyi et al., 1993). In the Espírito Santo Basin, halokinesis started in the Aptian–Albian and continued throughout the Cenozoic. It led to the development of discrete salt structures, and associated fault families, which were large enough to control the distribution and continuity of reservoir intervals in the Urucutuca Formation (Demercian et al., 1993; Fiduk et al., 2004) (Fig. 2). Hence, the structural framework of the Espírito Santo Basin comprises horsts and grabens below and Aptian evaporite unit, and supra-salt structures such as diapirs, salt rollers and rollovers, turtle anticlines, rafts and salt walls (Alves, 2012; Fiduk et al., 2004; Varela and Mohriak, 2013) (Figs. 2 and 3).

The aim of this paper is to describe the geometry and character of faults formed adjacently to three salt diapirs, and on the crest of a buried salt ridge, herein named as Salt Ridge (Fig. 4). We investigate the timing of formation of salt-related faults to conclude if they form at present, or formed in the past, structural corridors connecting distinct salt structures. The controls exerted by these fault corridors on fluid flow and strata compartmentalisation, under different stress regime(s), are assessed in detail. In summary, we aim at addressing the following research questions:

a) How does halokinesis influence fault families developed close to salt structures?

b) Are there any preferred directions to the reactivation of faults in the study area?

c) Is there a relationship between fault reactivation and the migration (or trapping) of fluids around salt structures?

d) How can the studied diapir systems provide insights into the evolution of the Espírito Santo Basin, contributing to the analysis of seal competence (and fluid migration) in the areas where halokinesis plays a central role?

This study is the first to determine a paleostress tensor for the Espírito Santo Basin, to model slip tendency and leakage factors for the interpreted faults, and to create juxtaposition diagrams to assess where fluids were more likely to migrate along (or across) faults. In the discussion section, an evolutionary model is proposed for the interpreted salt structures and related faults. This model addresses the timing(s) and relationship(s) between different fault families. The reasons for localised fault reactivation are also investigated and discussed in light of published work on different parts of the Espírito Santo Basin (e.g. Baudon and Cartwright, 2008; Omosanya and Alves, 2013; Ze and Alves, 2016). At the end of this paper, our results, and the integrated effects of halokinesis on the trapping and migration of fluids, are compared to areas with similar halokinetic structures.

2. Geological Setting

The Espírito Santo Basin comprises a rift basin developed in SE Brazil during the Late Jurassic-Cretaceous (Fig. 1). The basin covers an offshore area of ~ 200,000 km^2, while its continental part reaches 18,000 km^2 (Mohriak, 2003). Its northern limit is the Abrolhos Bank, a Paleogene volcanic plateau that separates Espírito Santo from the Cumuruxatiba Basin (Mohriak, 2005). The Vitória-Trindade High separates the Espírito Santo Basin from the Campos Basin to the south (França et al., 2007) (Fig. 1).

The tectono-sedimentary history of the Espírito Santo Basin comprises four evolution stages: pre-rift, syn-rift, transitional and drift (Cobbold et al., 2001; Ojeda, 1982). These four stages correlate with five depositional megasequences: pre-rift, rift, transitional, transgressive-marine and regressive-marine (Fiduk et al., 2004; Mohriak et al., 2008) (Fig. 3).

The pre-rift stage (Late Jurassic – Early Cretaceous) is associated with the Serra Geral magmatic event, which was initiated in the Paraná Basin and later reached areas of the continental margin such as the Espírito Santo Basin (Cainelli and Mohriak, 1999; Mohriak, 2003).

The syn-rift stage (Late Barresian - Early Aptian) is characterised by intense tectonism and corresponding formation of the East Brazil Rift System in response to divergent motion between South America and Africa (Chang et al., 1992; Demercian et al., 1993; França et al., 2007; Ojeda, 1982). In the syn-rift megasequence three main depositional systems were accumulated in narrow, fault-controlled depocentres generated between Espírito Santo and the Sergipe/Alagoas Basins to the north: 1) alluvial fans, fan deltas and transitional deposits, 2) lacustrine shales and marls, and 3) lacustrine pelecypod limestones (*coquinas*) (Cainelli and Mohriak, 1998). In the study area, the syn-rift megasequence is represented by the Cricaré Formation (Fig. 2; França et al., 2007; Vieira et al., 1994).

The end of continental rifting marks a transitional phase in the Espírito Santo Basin (Mohriak, 2003; Ojeda, 1982). The formation of a narrow and elongated basin, in an arid climate with little water circulation, promoted the accumulation of a thick evaporite megasequence during the Aptian (Mariricu Formation; Fig. 2). This megasequence forms the main seal unit above syn-rift strata (Chang et al., 1992; Demercian et al., 1993; França et al., 2007; Mohriak, 2003; Ojeda, 1982).

During the Late Cretaceous - Holocene drift stage, continuous subsidence resulted in the development of an open-marine setting (Bruhn and Walker, 1997; Cainelli and Mohriak, 1999; Mohriak, 2003). During the drift stage, the evaporitic (transitional) megasequence changed gradually into marine strata (Cainelli and Mohriak, 1998), and two megasequences were subsequently formed: the Early Drift Transgressive megasequence (Albian to Ypresian), consisting of dark shales, turbiditic sandstones and carbonate breccias from the Urucutuca Formation (Cainelli and Mohriak, 1998; França et al., 2007), and the Late Drift Regressive megasequence (Lutetian – Holocene), which comprises mixed siliciclastic and volcaniclastic units resulting from the erosion of the Serra do Mar and Serra da Mantiqueira mountains. Erosion of coastal mountain ranges occurred together with tectonic uplift and local volcanism on the Abrolhos Bank (Figueiredo and Mohriak, 1984; França et al., 2007; Mohriak, 2003) (Fig. 3). As a result, the volcaniclastic Abrolhos Formation became interbedded with thick turbidite intervals in the Urucutuca Formation during the late drift stage, particularly within channelised bodies whose distribution was controlled by halokinesis (Cainelli and Mohriak, 1998; Figueiredo and Mohriak, 1984; França et al., 2007; Mohriak, 2003) (Fig. 2).

Halokinesis, and the subsequent development of salt structures in the Espírito Santo Basin, was initiated in the Late Aptian-Early Albian in response to differential loading, gravity spreading and downslope thin-skinned gravitational gliding above Aptian evaporites (Demercian et al., 1993; Fiduk et al., 2004). Halokinesis generated structures such as salt pillows, salt rollers, vertical salt diapirs with overhangs, allochthonous salt tongues along contractional folds, salt canopies and tongues, turtle structures and large salt nappes (Fiduk et al., 2004; Strozyk et al., 2017) (Fig. 3). In the Espírito Santo Basin, the growth of salt structures continued through the Cenozoic as a result of: a) continued sediment transport onto the continental slope, and b) regional magmatism associated with the Abrolhos Plateau, two phenomena that resulted in continuous growth and deformation of pre-existent salt structures (Fiduk et al., 2004).

The study area is characterised by the occurrence of salt diapirs (Fig. 4). Post-salt strata were deformed by halokinesis during the Cenozoic (Alves, 2012; Alves et al., 2009; Baudon and Cartwright, 2008a), in association with three phases of fault growth (Baudon and Cartwright, 2008a; Omosanya and Alves, 2014). Halokinesis also resulted in the accumulation of thick, vertically stacked mass-transport deposits (MTDs) during the Middle Eocene - Early Miocene (Fiduk et al., 2004; Gamboa et al., 2010; Omosanya and Alves, 2013).

3. Data and methods

The interpreted 3D seismic volume covers an area of 1,670 km^2 within the Espírito Santo Basin, at a water depth ranging from 100 m to 1800 m (Fig. 1). The seismic data were pre-stacked time migrated with a 12.5 x 12.5 m grid line spacing, and acquired with a 6 x 5.700 m array of streamers. The data were processed in the time domain and zero-phased within a 2 ms vertical sampling window. Resampling at 4 ms with the application of anti-aliasing filter, TAU-P linear noise attenuation and TAU-P domain deconvolution preceded data processing. Three-dimensional pre-stack time migration used the Kirchhoff algorithm.

In this work, seismic data are displayed using the standard SEG convention for a zero-phase wavelet; an increase in acoustic impedance is shown as a red seismic reflection and a relative decrease in acoustic impedance is shown in blue. The vertical extent of the seismic survey is limited to 4.0 s Two-way travel time (TWTT). Average p-wave velocity data from Deep Sea Drilling Project (DSDP) Site 516 (Barker et al., 1983), located in the Santos Basin (Fig. 1), show values of 3100 m/s for the Late Cretaceous - Paleocene interval, and 2100 m/s and 1800 m/s for Eocene-Oligocene and Miocene-Holocene strata, respectively. These velocities were used to convert mapped faults and horizons to depth, and to obtain the true dip of faults. Based on the velocities for the DSDP Site 516, and a computed dominant frequency of 40 Hz, the vertical resolution of the seismic data was also estimated for distinct intervals. Considering a resolution limit of ¼ of the wavelength (λ) (Sheriff and Geldart, 1995), the Late Cretaceous – Paleocene interval has a vertical resolution of ~19 m, whereas the Eocene-Oligocene and the Miocene-Holocene intervals have vertical resolutions of ~13 m and ~11 m, respectively.

Ten (10) key seismic reflections, including the seafloor, were mapped in this work at a spacing of ten lines (125 m). Smaller intervals of 1-5 lines (12.5 to 62.5 m) were used to map salt diapirs as discrete structures. Based on the published DSDP well data for SE Brazil, published seismic-stratigraphic frameworks (Alves et al., 2009; Fiduk et al., 2004; Gamboa et al., 2012; Gamboa and Alves, 2015; Viana et al., 2003), and the character and geometry of the interpreted seismic reflections, we defined three principal units in the study area: Late Cretaceous – Paleocene (Unit 1), Eocene – Oligocene (Unit 2), and Miocene – Quaternary (Unit 3). (Fig. 3, Table 1). Structural maps of horizons H_1, representing the top-salt horizon, and H_6 (corresponding to the Mid-Eocene unconformity that bounds Unit 1 at the top), are shown in this paper (Fig. 5).

3.1. Structural analyses

Variance time-slices were used to map distinct fault families around salt structures based on their geometry, orientations, and relationship with main structural features. Variance data are computed by converting a seismic-amplitude volume into a discontinuity volume, thus highlighting the most prominent discontinuities in a 3D seismic volume, including faults and fractures (Brown, 2011).

Two hundred and fifteen (215) faults were manually mapped every inline (12.5 m), and every five crosslines (62.5 m). The mechanisms of initiation, growth, and propagation of faults can be depicted using displacement data (e.g. Baudon and Cartwright, 2008; Cartwright and Mansfield, 1998). In detail, the relationship between the maximum displacement (D_{max}) and the length (x) of a fault trace is the basis for displacement-length (D-x) analyses (Cowie and Scholz, 1992; Muraoka and Kamata, 1983; Nicol et al., 2002; Peacock and Sanderson, 1991). In this work, displacement was measured for twelve (12) representative faults at a pre-defined cut-off horizon. Displacement and distance data, originally in ms TWTT, were converted into metres. Plots of maximum displacement (D_{max}) against length (x), compiled for all faults in the study area, were then compared to published data (e.g. Muraoka and Kamata, 1983; Scholz and Cowie, 1990; Walsh et al., 2002; Walsh and Watterson, 1987) for normal, strike-slip and reverse faults using the *Fault Analysis Module* in Midland Valley Move®.

The relationship between fault throw (T) and depth (z) is widely used to estimate fault reactivation (Baudon and Cartwright, 2008a, 2008b; Cartwright and Mansfield, 1998; Mansfield and Cartwright, 1996). Throw-depth (T-z) profiles for reactivated faults show abrupt variations in throw gradient and values, whereas minor changes (and comparatively smaller throw values) are obtained for non-reactivated faults (Baudon and Cartwright, 2008a). In this work, we show throw-depth relationships for the 12 representative faults previously mentioned using seismic profiles that are orthogonal to the fault strikes, and measuring the vertical offset between hanging-wall and footwall cut-offs (Baudon and Cartwright, 2008a; Mansfield and Cartwright, 1996; Mattos et al., 2016; Omosanya and Alves, 2014). The resulting T-z profiles were created in Microsoft® Excel, with values displayed in two-way travel time (ms TWTT).

Displacement analyses were carried out so that faults and horizons interpreted in Petrel® could be imported into Midland Valley Move® as 3D mesh surfaces, and later filtered for edge triangles. Key fault attributes, including true dip, strike and azimuth for each fault vertex, were created in Move® using the *Attribute Analyser Toolbar*. Fault analyses performed in this paper included the creation of juxtaposition diagrams and stress analyses.

Stratigraphic juxtaposition is a widely-applied method to predict the potential of fluid retention and migration through faults (Allan, 1989; Knipe, 1997; Reilly et al., 2016). The juxtaposition of impermeable strata, such as shales, against permeable units (sandstones), can create an effective seal. In contrast, the juxtaposition of permeable units is likely to promote cross-fault lateral migration. We used the *Fault Analysis Module in Move®* to create hanging-wall and footwall cut-off lines for stratigraphically-assigned seismic horizons using a trim distance of 15 m. Juxtaposition diagrams (Allan diagrams) were created for the 12 representative faults considered in this work.

Stress analyses were performed to assess the orientation and distribution of the principal paleostress tensors associated with the 12 representative faults using the *Stress Analysis Module* in Move®. The paleostress inversion method is based on the relationship between slip-tendency values and displacement measured for a set of faults (McFarland et al., 2012). Fault slip tends to occur if shear stress is equal or greater than the normal stress acting on a fault surface (Morris et al., 1996). Two important criteria must be taken into account when assessing the inverted stress tensor: a) a positive relationship between the slip tendency and displacement is expected, and b) surfaces with high slip tendency and large displacements indicate an early slip, whereas small displacements indicate that the fault slip started at a later time (McFarland et al., 2012). Once we obtained the paleostress azimuths and magnitudes, we modelled the slip tendency and the leakage factor using the *Stress Analysis Module* for the faults in the study area.

Slip tendency (T_s) is defined as the likelihood of a fault to slip, and is estimated as the ratio of shear (τ) to normal (σ_n) stresses on a fault plane (Equation. 1; Morris et al., 1996). Slip tendency has no units and is mathematically written as:

$$T_s = \frac{\tau}{\sigma_n{}'}$$

Eq. (1)

Slip tendency is dependent on the orientation of a fault surface and the stress field acting on it. A fault will slip according to the cohesive strength of its surface, and the coefficient of static friction (μ). Slip for a cohesionless fault surface will occur when the resolved shear stress is equal or exceeds the frictional resistance to sliding (F), as shown in Equation 2 (Morris et al., 1996):

$$F \leq \tau = \mu\sigma_n$$

Eq. (2)

The fluid transmissivity of faults can be modelled by estimating a Leakage factor (L). Faults that either constitute migration conduits for fluids in the subsurface, or act as local seals, can be estimated quantitatively on colour-scaled 3D maps of fault planes. Leakage factor is defined as the ratio of the fluid pressure (P_f) to the difference between the normal stress (σ_n') and the tensile strength (T) of a fault zone (Equation. 3; Morris et al., 1996) such as:

$$L = P_f/(\sigma_n' - T)$$

Eq. (3)

The magnitudes and azimuths obtained from our paleostress analysis were used together with a fluid pressure (P_f) value of 9 MPa, obtained from the locally estimated vertical stress, and considering both the depth of the unit of interest and the water column above the seafloor (Zoback, 2010).

Fault reactivation must be taken into account when assessing the leakage potential of a reservoir interval. Methods to assess the risk of breaching seal units by the juxtaposition of permeable strata across faults include detailed assessments of fault geometry and the use of in-situ stresses (Ferrill et al., 2009; Jones and Hillis, 2003; Morris et al., 1996). However, the absence of borehole breakout data for the Espírito Santo Basin made necessary the use of paleostress data, and juxtaposition diagrams, to provide evidence for reservoir compartmentalisation associated with fault reactivation.

4. Seismic stratigraphy of the Espírito Santo Basin

4.1. Unit 1 (Albian– Middle Eocene)

Unit 1 is the primary unit of interest in this paper (Figs. 4 and 6 to 8). Unit 1 comprises sub-units 1a to 1e. It is bounded at its base by horizon H_1 and at its top by a Mid-Eocene unconformity defined by horizon H_6 (Figs. 4 and 6 to 8). Sub-unit 1a is bounded at its base by horizon H_1 (Figs. 4 and 6 to 8), a moderate- to high-amplitude negative reflection, and at its top by the moderate-amplitude (and nearly continuous) horizon H_2 (Figs. 4 and 6 to 8). Low-amplitude to transparent seismic reflections predominate in this sub-unit. Its thickness ranges between 200 – 500 ms, decreasing on the flanks of salt structures. Sub-unit 1a is likely composed of distal turbidites and shale-rich carbonates (Alves et al., 2009; Fiduk et al., 2004; Viana et al., 2003).

Horizon H_2 delimits the base of sub-unit 1b. The upper boundary of this 75 ms- to 175 ms-thick sub-unit is defined by horizon H_3 (Figs. 4 and 6 to 8). The sub-unit is offset by faults that are radial to the smaller salt diapirs, and by faults developed on the Salt Ridge (Figs. 4 and 6 to 8). The internal character of sub-unit 1b becomes chaotic in the proximity of the Rio Doce Canyon System (Fig. 4). In the area of interest to this study, sub-unit 1b is characterised by moderate-amplitude, sub-parallel seismic reflections that reflect an increase in sand volume relative to sub-unit 1a.

Sub-unit 1c is defined at its base by horizon H_3 and at its top by horizon H_4 (Figs. 4 and 6 to 8). This sub-unit consists of a 25 ms-thick, moderate amplitude package interpreted as shale. Horizon H_4 delimits the base of Sub-unit 1d, which comprises a 40 ms-thick package with moderate amplitude. The amplitude of this sub-unit increases close to diapirs and salt-ridge crests due to a relative increase in sand content.

Horizon H_5 delimits the base of sub-unit 1e, a 75 ms- to 175 ms-thick package delimited at its top by a regional erosional unconformity; horizon H_6 (Figs. 4 and 6 to 8). Sub-unit 1e comprises transparent to low-amplitude internal reflections, which become chaotic close to diapirs and the Rio Doce Canyon System. This sub-unit is likely composed of fine-grained (clayey) turbidites. Close to the Rio Doce Canyon System, these fine-grained units alternate with sand-rich turbidites (Alves et al., 2009; Viana et al., 2003). The majority of faults in the study area are truncated by horizon H_6 at their upper tips (Figs. 4 and 6 to 8).

4.2. Unit 2 (Middle Eocene – Early Miocene)

Unit 2 is delimited at its base by a Mid-Eocene unconformity, horizon H_6 (Fig. 5b). Faulting is ubiquitous at this level, but rarely propagates into the upper part of Unit 2 (Figs. 4 and 6 to 8). Unit 2 consists of chaotic low-amplitude to transparent reflections intercalated with moderate amplitude strata. The base of Unit 2 (sub-unit 2a) is characterised by blocky mass-transport deposits (MTDs) accumulated around a buried salt ridge developed between diapirs D1 and D2 (Gamboa and Alves, 2015). Blocks are moderate-amplitude features with sharp to smooth edges (Figs. 4 and 6 to 8). The middle and upper parts (sub-units 2b and 2c) of Unit 2 are characterised by the occurrence of high-amplitude seismic reflections previously interpreted as sand-rich turbidite lobes (Alves et al., 2009; Gamboa and Alves, 2015). These two sub-units are separated by horizons H_7 and H_8 (Figs. 4 and 6 to 8). The upper boundary of Unit 2 is defined by the Early Miocene horizon H_9 (Figs. 4 and 6 to 8).

4.3. Unit 3 (Miocene – Quaternary)

The base of Unit 3 coincides with Horizon H_9, whereas the sea floor delimits its top. Unit 3 is characterised by low-amplitude, sub-parallel seismic reflections incised by submarine channels (Figs. 4 and 6 to 8). Submarine channels are deformed close to salt diapirs (Figs. 4 and 6 to 8). Unit 3 includes interbedded sand, shale-rich turbidites and hemipelagic sediment (Fiduk et al., 2004; Viana et al., 2003).

5. Fault distribution around salt structures

In agreement with previous work by Fiduk et al. (2004), Gamboa, (2011) and Gamboa and Alves (2015), we interpret the salt structures in the studied area as rooted on the NW-trending Salt Ridge. This Salt Ridge shows a maximum width of ~ 2.7 km and a length of 10 km, merging at depth with diapir D1. The Salt Ridge forms an anticlinal structure with a lenticular shape (Figs. 6a and 6b). In contrast to adjacent salt structures, Units 1 to 3 bury the Salt Ridge and faults are well developed on the crest of this structure.

Diapir D1, located in the eastern part of the study area, has a diameter of ~ 5.4 km (Fig. 8). Diapir D1 penetrates the post-salt overburden to a depth ~ 400 ms below the sea floor, deforming Units 1 to 3 (Fig. 8). Diapir D2 shows a diameter of 2.6 km and is the smallest diapir in the study area. It penetrates through Units 1 and 2 and partially through Unit 3 (Fig. 7). Diapir D3 occurs in the NW part of the study area and shows a diameter of ~ 7.1 km. Over diapir D3, salt has deformed the three stratigraphic units to reach the sea floor (Fig. 6a).

Structural interpretations based on the analysis of seismic profiles (Figs. 4 and 6 to 8) combined with variance time-slices (Fig. 9) allowed us to subdivide the imaged faults into five (5) families based on their position relative to the principal salt ridge and adjacent diapirs.

5.1. Faults on the Salt Ridge

The preferential trend for the 55 faults mapped over the buried Salt Ridge is NW-SE (Fig. 10a). This trend corresponds to 72% of the faults developed on the ridge, including F1 and F12 (Fig. 10a). The NW-striking faults in the Salt Ridge are longer than their NE-striking counterparts (Fig. 9). The average length of the faults in the salt ridge is 1.2 km. Faults dip both to the NE and SW (Fig. 10a).

One of the most distinctive features of this family of faults is the occurrence of fault F1, the largest in the study area, with a length of 9.5 km. Fault F1 is parallel to the salt ridge and terminates to the NE of diapir D1 (Fig. 9). Fault 12 occurs to the north of D1. Faults F1 and F12 follow the same direction of the Salt Ridge and are confined to Unit 1, with no evidence of faults reaching the MTDs in Unit 2 (Figs. 6a and 6b). Tilt blocks formed at the crest of the buried ridge do not show growth strata on the seismic sections (Figs. 6a and 6b). Distinctive bright reflections occur between -3280 and -3420 ms, in Sub-Unit 1c (Fig. 6b).

5.2. Diapir 1 (D1)

Fifty-three (53) faults were mapped around diapir D1 to show a radial distribution (Fig. 9). Approximately 57% of the mapped faults have a NW trend over D1, whereas the remaining 43% trend to the NNE (Fig. 10b). Faults around D1 dip preferentially to the NE, showing an average dip of 32º. Representative faults include F2, F3, F8 and F9 (Fig. 9). Most faults occur between horizons H_2 and H_6. However, an important number of faults also offset horizon H_1, including F2 and F9 (Fig. 6b).

One of the most striking features around D1 is fault F3, a NW-trending structure with an average dip of 41º, offsetting horizons H_2 to H_9 along its length (Fig. 7). Fault F2 is NNE-striking, terminating against the Salt Ridge. A sucession of tilt-blocks is observed on the crest of D3 (Figs. 8a and 8b) and radially to D1 (Fig. 8a). Radial faults include fault F9, a 3.3-km long NW-striking structure that extends towards D3 (Fig. 9). Next to D1, NW-striking faults occur and bright reflections are observed in strata offset by fault F8 (Fig. 8a).

5.3. Southern area

The southern part of the study area is the most faulted in the study area, with 77 faults (Fig. 9). Here, faults do not have a radial distribution; the preferential orientation is NW-SE for 36% of these faults, while the least common strike is to the SW for 19.7% of the faults (Fig. 10c). By comparing the faults mapped in the southern area with those around the salt diapirs we observe that the former are smaller in length (average length 0.8 km) and limited to Unit 1 (Fig. 8). Some of the faults propagate from the Aptian salt, reaching depths of -3880 ms. However, none of the faults offset the Mid-Eocene unconformity (horizon H_6) or extend into Unit 2 (Fig. 8). On the variance maps, faults mapped in the southern part have polygonal distributions (Fig. 9). The southern area shows a greater concentration of bright reflections along fault blocks compared to other parts of the seismic volume (Figs. 8a and 8b).

5.4. Diapir 2 (D2)

Eleven (11) faults were mapped around diapir D2, and data plotted on the rose diagram in Figure 10d, show a radial distribution with 75% of the faults varying in strike between 180º and 360º. The average dip for these faults approaches 30º. Although most of these faults are observed in Unit 1, some structures close to D2 (including fault F7) offset the top of the Aptian salt (horizon H_1) and terminate in sub-unit 2b (Figs. 7 and 8b). Away from D2, the NE-striking fault F7 offsets horizons H_2 to H_5 (Fig. 7). A bright reflection occurs close to diapir D2, on the footwall of fault F6 (Fig. 7).

5.5. Diapir 3 (D3)

Nineteen (19) faults were mapped around diapir D3, and show a radial distribution (Fig. 9). Approximately 46% of the faults strike to the NW, and 22% of the faults strike to the SW (Fig. 10). Faults radial to D3 include both synthetic and antithetic faults (Fig. 8). Most of the faults occur between horizons H_2 and H_6, on the crest of D3, and rarely offset horizon H_1. A distinctive feature around D3 is the occurrence of faults offsetting the base of MTDs in sub-unit 2a (Figs. 6b, 8a and 8b). The average length for this group of faults is 1.6 km, with representative faults F10 and F11 striking to the NW (Fig. 9). Bright reflections are observed close to faults radial to D3 (Fig. 8). A large number of bright reflections are also found above faults in Unit 2 (Figs. 6b, 8a and 8b).

6. Fault displacement analysis

6.1. Interpretation of distance-length (D-x) profiles

Displacement-length (D-x) plots were compiled for the twelve (12) representative faults using horizon H_5 as reference (Fig. 11). The geometry of the D-x profiles relates to the observed displacement variations along the total length of a fault. For single and isolated faults, D-x profiles represent a near-symmetric slope with gentle variations in displacement and flat-topped curves, which are characteristic of C-type faults (Childs et al., 1995; Muraoka and Kamata, 1983; Nicol et al., 1996; Peacock and Sanderson, 1991). Complex D-x profiles result from the presence of abrupt variations in displacement along faults, a character indicating linkage of individual fault segments associated with displacement minima during fault growth (Walsh et al., 2003). These structures are classified as M-Type faults (Muraoka and Kamata, 1983), and their characteristic profiles show a broad central section with no significant slope variations. Their tips show abrupt displacement variations, resulting in a marked asymmetric character on D-x plots. Displacement maxima relate to the first nucleation point for individual fault segments (Barnett et al., 1987; Nicol et al., 1996; Walsh and Watterson, 1987). This assertion, however, is only true for non-segmented or isolated blind faults.

Overall, the geometry of the D-x profiles varies from asymmetric (F1, F5, F6, F7, F9, F10 and F11) to symmetric (F2, F3, F4, F8, and F12). Faults F3 and F4 have distinctive M-type profiles. In detail, F5 is skewed to the east, whereas F6 is skewed to the northwest. The remaining faults have more complicated displacement profiles. Faults F4 and F7 for example, are a combination of C-type profiles on the left (NE and W, respectively) and an M-type profiles on their right (SW and E, respectively) (Fig. 11). Faults F6, F7, F8 and F10 terminate at the edge of the salt diapir, and no nil displacements values were observed at such point (Fig. 11). Two near-flat profiles seem to be the preferential D-x geometry for fault F9. Faults F1, F11 and F12 have the most complex displacement profile, with a succession of several C-, M-, and skewed-type profiles (Fig. 11).

Fault geometries are more complex around the Salt Ridge and D3 when compared to the remainder of the study area. The complexity of these D-x profiles indicates that faults formed around salt structures were not fully isolated during their propagation and growth. However, the presence of displacement minima indicate that fault development in the study area is a combination of initially isolated fault segments, which grew laterally to a maximum length to become constant-length faults (*cf.* Childs et al., 1995; Peacock and Sanderson, 1991). Fault F2 is the only fault in the study area with an overall shape resembling the C-type profile of Muraoka and Kamata (1983).

A relationship between fault segmentation and fault length can be established considering that large faults such as F1 (9.5 km), F11 (5.5 km) and F12 (3.8 km), appear to be the most segmented structures in the study area. They show clear displacement minima, whereas in small faults such as F4 (1.4 km) and F8 (750 m), variations in displacement seem to be less significant. For the remaining faults, the number of segments varies with fault length at different scales. In addition to fault segmentation, representative faults also have variable maximum displacement (d_{max}) and fault length (Fig. 11). Values of D_{max} range from 82.83 m (F1) to 36.75 m (F8), while fault length varies from about 750 m (F8) to 9.5 km (F1).

6.2. Interpretation of throw-depth (T-z) profiles

Throw-depth (T-z) plots for the 12 representative faults are shown in Fig. 12. Throw profiles in the study area include M- (F1, F2, F6, F9) and C-types (F4, F5) *cf.* Muraoka and Kamata (1983). Fault F3 is an example of a skewed M-type profile. Often, the T-z profiles of some faults show a hybrid character that results in the combination of two or more throw profiles. Fault F7 consists of a combination of M- and C-types in Unit 1, whereas an M-type profile is observed in Units 2 and 3. The throw profiles for faults F10 and F12 show a combination of M- and C-types profiles. Faults F8 and F11 consist of two M-type profiles (Fig. 12).

Throw minima and maxima vary significantly across seismic horizons and at depth. The position of throw minima and maxima across stratigraphic levels appears to relate to fault segmentation and reactivation by dip-linkage (Baudon and Cartwright, 2008a; Omosanya and Alves, 2014; Walsh and Watterson, 1989). For faults F2, F4, F9, F10, F11 and F12, a significant reduction in throw values occurs at horizon H_2 (Fig. 12). Faults F1, F6, F7 and F8 show distinct throw minima within sub-unit 1a. A second negative displacement is recorded close, or at horizon H_5, for faults F1, F3, F5, F7, F8, F11 and F12. Throw maxima occur at sub-unit 1e, delimited by horizons H_5 and H_6, for faults F2, F3, F6, F7, F9, F10 and F12, while for fault F1 maximum throw occurs at horizon H_5 (Fig. 12). The position of the throw maxima in the analysed faults implies nucleation of the faults in sub-unit 1e.

The maximum throw recorded for the faults in the study area is 50 ms for fault F5. Compared to the other faults, F8 show a distinct throw profile, characterised by small throw values close to the upper tips of the fault and increase with depth, whereas the majority of the faults seem to show a relative decrease i with depth.

Displacement ideally decreases to zero towards fault tips, a character reflecting their propagation towards a free surface, and increases to a maximum in the centre of the fault surface (Childs et al., 2003; Kim and Sanderson, 2005; Walsh and Watterson, 1988). However, most of the faults in the study area show significant displacement on their upper tips, reflecting near-sea floor erosion at the time of their propagation. The faults studied in this paper are truncated by the Mid-Eocene unconformity (horizon H_6) on the seismic sections (Figs. 3 and 6 to 8). Exceptions to this pattern include faults F3 and F7, both propagating above the Mid-Eocene unconformity and reaching Unit 3. For fault F3, its upper tip is truncated by a submarine channel in Unit 3 (Fig. 7). The T-z profiles for these two faults show an abrupt displacement shift to the left at the horizon H_6 (Fig. 12), followed by an increase in throw at shallow levels, indicating the occurrence of a reactivation episode. Considering that faults F3 and F7 are located adjacent to diapirs D2 and D3, it is possible to suggest that fault reactivation occurred in response to the growth of these salt structures. Halokinesis did not affect the upwards propagation of other faults in the study area, as they chiefly terminate at the base of the MTDs in Unit 2, i.e. below the Mid-Eocene horizon H_6 (Fig. 12).

7. Stratigraphic juxtaposition

The displacement of permeable and impermeable units across fault planes can be graphically represented by Allan Diagrams (Allan, 1989). Juxtaposition (Allan) diagrams were created for faults F1 to F12 by assigning stratigraphic intervals as salt, limestone, shale, silt and sand to the interpreted seismic units and sub-units (Fig. 13). In the salt ridge, we estimate the juxtaposition of sands in the central part of fault F1 (Fig. 13a). This permeable interval is delimited laterally, and at its top, by a relatively thin shale interval. For fault F1, we observe juxtaposed limestone-limestone intervals, together with and sand-shale and sand-silt contacts.

Fault F2, around diapir D1, has a juxtaposition diagram similar to F1 with sand units delimited vertically and laterally by impermeable units (Fig. 13b). Distinctive shale-silt and shale-sand juxtapositions are observed at the centre of this fault. Towards the Southern Area, the juxtaposition diagram for fault F5 shows an upper sand body laterally delimited by silt to the west (Fig. 13c).

The complex geometries of faults located adjacent to diapir D2 are illustrated by the juxtaposition diagram for fault F7 (Figs. 13d). Fault F7 shows a sand-silt juxtaposition in its upper tip towards the west (Fig. 13d). This fault was reactivated towards the east, where juxtaposed sand bodies are not delimited laterally by impermeable units. The lowermost sand interval is delimited by a sand-silt contact to the west and by a shale-silt juxtaposition to the east (Fig. 13d).

Fault F9, adjacent to diapir D1 displays complex juxtaposition of strata (Fig. 13e). The diagram for fault F9 shows a silt-silt juxtaposition at the NW and SE fault terminations, isolating the sand body. Shale-sand and shale-silt contacts are also observed (Fig. 13e). No impermeable (lateral) juxtapositions are observed for faults located adjacent to diapir D3 (Figs. 13f). Fault F11 shows a sand-sand contact delimited vertically by a silt-silt juxtaposition increasing in thickness towards diapir D3. Shale-shale, shale-sand and shale-silt contacts are observed under the sand interval (Fig. 13f).

8. Stress analyses

The existence of only one earthquake focal mechanism in the Espírito Santo Basin, close to the Victoria-Trindade High, the limited seismological coverage in the study area, and the low number of stress measurements for SE Brazil's offshore basins, hinder the determination of a regional stress tensor for the Espírito Santo Basin (Lima et al., 1997). Furthermore, post-salt deformation is considered to be gravitationally driven, and independent of any basement tectonics (Demercian et al., 1993).

The faulting styles and tectono-stratigraphic evolution of the Espírito Santo Basin point towards an extensional regime in the study area (Chang et al., 1992). Stress inversions for a set of 215 faults in the study area confirm Chang et al. (1992) interpretation by computing a sub-vertical σ_1 plunging -57.89º along an N237.63º azimuth (Table 2). A sub-horizontal σ_3 plunging 17.34º along an N177.46º azimuth was also estimated. Considering that halokinesis resulted, in the study area, in the development of faults with more than two preferential strike directions, we used the results from stress inversions for the faults located in the Salt Ridge to perform slip tendency and leakage factor analyses for the remaining faults F1 to F12. Faults over the Salt Ridge show a more uniform strike and dip distributions when compared to F1 to F12 (Fig. 10). Stress inversions in the Salt Ridge indicate a sub-vertical σ_1 plunging -52.7º along an N187.1º azimuth and a sub-horizontal σ_3 plunging 33º along an N218.6º azimuth (Table 2).

Slip tendency values based on the stress tensor for the Salt Ridge vary from 0.03 to 0.82, showing an average of 0.53 (Fig. 14). The largest slip tendency values, varying from 0.50 to 0.82, are recorded for NW-striking faults, whereas slip tendency ranges from 0 to 0.46 for NE-striking faults (Fig. 14). A similar slip tendency is observed close to D1, with values varying from 0.3 to 0.8 for NW-striking faults and values from 0.0 to 0.3 for faults striking to NE. For the faults in D2, slip tendency ranges from 0.06 to 0.50, with an average slip tendency of 0.34. Most of the faults located around D3 have slip tendency values ranging from 0.02 to 0.25, with NW-striking faults showing the largest slip tendency, from 0.4 to 0.75.

Normalised leakage factors were also estimated considering a fluid pressure of 9 MPa, based on vertical stress measurements (see Zoback, 2010) (Fig. 15). Leakage factor varies from 0.27 to 0.85, indicating a medium to high capacity of faults to leak fluid. Most faults have leakage factors ranging from 0.32 to 0.54, whereas the largest leakage factors, ranging from 0.65 to 0.85, occur in faults in the southern part of the study area (faults F4 and F5) and radial to D3 (Faults F10 and F11). Faults F8 and F7, show distinct leakage factors to the rest of the faults adjacent to D1 and D2 (Fig. 15). Importantly, leakage factors are greater for NW-trending faults than for their NE-striking counterparts (Fig. 15).

9. Discussion

9.1. Structural evolution of the salt structures and timing of faulting

A 3D representation of the interpreted faults in the Espírito Santo Basin is shown in Fig. 16. In order to constrain the timing of faulting, we used horizon H_6 as a time marker. Two main episodes of faulting, pre-Mid-Eocene and post-Mid-Eocene, are defined based on the interpreted stratigraphic relationships between Cretaceous and Paleogene strata, and Throw-depth (T-z) plots for the representative faults F1 to F12.

An important observation on seismic data is the absence of thickness variations on the hanging-wall and footwall blocks of F1 to F12, suggesting that faulting was initiated in the study area after the deposition of Unit 1 (Albian – Middle Eocene, Figs. 4 and 6 to 8). At a regional scale, the first halokinetic movements in the Espírito Santo Basin took place during the Aptian – Albian, resulting from the combination of differential sediment loading, gravity spreading and downslope thin-skinned gravitational gliding above Aptian evaporites (Demercian et al., 1993; Fiduk et al., 2004). Considering the geometry of the interpreted seismic sections (Figs. 4 and 6 to 8), we agree that halokinesis spanning the Aptian to Albian time period deformed post-salt overburden units in the Espírito Santo Basin. However, this deformation was not continuous, and discrete episodes of faulting occurred before the Mid-Eocene as identified in this study. Such an observation agrees with the discrete (and localised) salt deformation that took place in the South Atlantic continental margins during the Albian, Campanian, Paleogene and Neogene (Cobbold et al., 2001; Fiduk and Rowan, 2012; Quirk et al., 2012; Strozyk et al., 2017).

The interpreted seismic cube reveals faults propagating on the crest of salt structures (Figs. 4 and 6 to 8). Faults offsetting salt structures (horizon H_1) include F1, F2, F9 and F11, located at the crests of the Salt Ridge and diapirs D1 and D3 (Figs. 6 and 8). Throw-depth (T-z) data for these faults indicate that a first episode of reactivation occurred in the Albian, as recorded by the throw minima around horizon H_2 (Fig. 12). Away from salt diapirs, seismic reflections seem to be less deformed towards the southern part of the study area (Fig. 6). The relative absence of the salt towards the south, and the occurrence of faults with a throw minima at horizon H_2 (e.g. fault F4), confirm that extension took place during the Albian – Early Eocene.

In faults F10 and F11, the throw minima at horizon H_3 suggest a second reactivation episode close to diapir D3 (Fig. 12). Halokinesis is also apparent for the Salt Ridge and diapirs D1 and D2, as reflected by the displacement minima close to horizon H_5 (sub-unit 1e). We interpret this episode of salt movement as the last halokinetic event recorded on the Salt Ridge, as this structure is now buried by a non-deformed post-salt overburden (Units 2 and 3). Cessation of salt growth resulted in local dissolution of the crest of the Salt Ridge, as shown by the lenticular shape of this salt body on the seismic sections (Fig. 6). The removal of salt occurred preferentially on the crest of salt structures where the salt rises faster, and continued towards the diapir flanks (Ge and Jackson, 1998; Seni and Jackson, 1984).

Despite salt dissolution and the pressure exerted by overburden units on the Salt Ridge, no evidence of collapse as in Frumkin et al., (2011), Ge and Jackson, (1998) or Mattos et al., (2016), is observed in the 3D seismic volume for this same structure. This finding contrasts with observations for the eastern part of this seismic volume, where salt withdrawal and collapse play a major role in fault evolution (Alves et al., 2009; Ze and Alves, 2016). Throw-depth (T-z) data for the 12 representative faults, show that displacement decreases towards the Mid-Eocene horizon H_6 (Fig. 12). However, throw for these faults is always greater than zero, as it does not represent the cessation of vertical propagation, hence confirming the removal of part of the Mesozoic strata in the study area(Fig. 12).

Our interpretation shows that the bulk of halokinetic movements occurred during the Middle Eocene – Early Miocene, as reflected by the local growth of diapirs D1, D2 and D3. The thinning and folding of Units 1 and 2 on the flanks of salt diapirs reflect post-depositional halokinesis (Figs. 4 and 6 to 8). However, this halokinetic episode had little influence on fault reactivation. No faults were found on the crest of the salt structures, and only a few faults were reactivated after the Mid-Eocene in the western part of the study area. Hence, reactivated faults crossing horizon H_6 include F3, adjacent to D1, and F7 adjacent to D3. Throw profiles for these two faults are similar, evidencing a decrease in the throw values for Units 2 and 3 towards their upper tips (Fig. 12).

9.2. Mechanisms of fault linkage and reactivation

Displacement profiles in sections 6.1 and 6.2 provide insights into the mode of propagation and linkage of faults in the western part of the Espírito Santo Basin. Fault geometry and its relationship to adjacent strata are also taken into account when proposing the evolutionary model in this work. For the majority of representative faults, throw-depth (T-z) data show a throw maxima close to horizon H_5 (Fig. 12). These faults developed radially to diapirs D2 and D3 (Fig. 11), and in map view radiate out from the diapirs in the direction of other salt structures, where the faults overlap (Fig. 9). Faults developed radially to D1, and the crestal faults in the Salt Ridge seem to be more segmented than those around D2 and D3 (Fig. 11). Extension causing the uplift of the Salt Ridge was likely involved in the linkage of the individual fault segments, whereas the successive halokinetic movements of D3 were likely responsible for lateral and vertical propagation of faults that are radial to this structure. Growth in diapirs D1 and D2 are also responsible for the lateral segmentation of faults adjacent to these structures.

Multiple displacement minima for the faults radial to diapirs (e.g. F3, F7, F10 and F11) indicate that these faults consist of multiple vertically overlapping segments (Fig. 12). For the majority of the representative faults, throw minima occur in sub-unit 1a. The throw-depth profiles indicate larger throw for faults in the western portion of the study area than for the crestal faults found in the eastern part (e.g. Baudon and Cartwright, 2008a). As displacements are larger in the western part of the study area, characteristic throw minima are also observed. The occurrence of successive throw minima on the T-z plots suggests dip-linkage reactivation (Baudon and Cartwright, 2008a; Mansfield and Cartwright, 1996; Omosanya et al., 2015). Dip-linkage reactivation is less common for the faults generated in the eastern part of the study area, as these were chiefly reactivated by upward propagation (Baudon and Cartwright, 2008a). Towards the west, dip-linkage seems to be the preferential reactivation mode, with upwards propagation being relatively moderate.

Possible explanations for the different modes of reactivation found in the study area include: a) distinct relationships between fault strike and local stress states, and b) radial faults were formed after salt diapir growth, whereas crestal faults propagated in association with regional extension. The orientation of the principal stresses estimated by inverting the faults on the Salt Ridge is NE-SW (Table 2), agrees with the NNE-trending extension direction suggested by Chang et al. (1992) for the SE Brazil. Wherever the orientation of the principal stresses and the strike direction of faults is coincident, there is a greater tendency for faults to reactivate vertically along their length (Baudon and Cartwright, 2008a; Ze and Alves, 2016). The predominant strike direction for the faults in the western part of the Espírito Santo Basin is NW-SE. However, important groups of NE-SW and E-W faults are also found in the study area. In general, the representative faults striking to NNE-SSW display a variable number of throw minima on their throw profiles, whereas NW-SE and E-W striking faults show two negative displacements on their profiles (Fig. 12). Opposing strike and principal stress orientations can, as a result, control the preferential fault reactivation mode, favouring the nucleation of segments with similar dip and strikes.

Faults F3 and F7 are the only representative faults that, after a negative break on the throw gradient at the Mid-Eocene horizon H_6, propagated vertically into Units 2 and 3. Faults F3 and F7 strike in opposite directions, NW-SE and NE-SW, respectively. While T-z data for fault F3 indicates a gradual reduction in throw above horizon H_6, fault F7 shows at least six throw minima along its throw profile

(Fig. 12). The T-z for these two faults are an exception to the general pattern of fault growth and evolution observed to the faults in the study area. This indicates that not only regional stress orientations should be considered when assessing fault reactivation, but other local factors, including the presence of overlapping faults (Childs et al., 1995; Kelly et al., 1999) and fault size (Peacock and Sanderson, 1996, 1991), should also be taken into account.

9.3. Implications for petroleum systems in the Espírito Santo Basin

A dense and connected fault network can either constitute a preferential conduit to fluids (Cox et al., 2001; Gartrell et al., 2004) or form barriers to fluid flow as result of shear processes or post-deformation cementation (Gartrell et al., 2003; Sibson, 1996). Crestal and radial faults in the study area comprise corridors connecting distinct salt structures that discretely evolved through time in the Espírito Santo Basin (Fig. 16). The juxtaposition (Allan) diagrams for the study area indicate that faults located radially to D2 and D3, and those located to the south, comprise thicker juxtaposed sands when compared to faults formed close to D1 and the Salt Ridge (Fig. 13). Such an observation is complemented by the presence of bright spots on seismic data. The largest and most continuous bright spots were found in sub-unit 1e adjacently to faults developed radially to diapirs D2 and D3 (Figs. 7 and 8). Faults F9 and F10 offset a bright-spot, meaning these faults can either constitute a possible pathway for fluids or form local seals (Fig. 8). Slip tendency and leakage factor values indicate that F9 could potentially form a competent seal, whereas fault F10 would facilitate fluid flow (Figs. 13 and 14). Bright-spots were also identified at Unit 2, above the faults radial to D3, whereas in the Salt Ridge bright reflections predominate above faults offsetting sub-units 2b and 2c (Fig. 6).

Fault zone complexity limits the analysis of fault-seal behaviour and associated fluid flow paths based solely on seismic data. In fact, important parameters such as the amount and distribution of smeared shales across a fault (Manzocchi et al., 2010), can be overlooked when borehole data are not available (e.g., Caine et al., 1996; Fisher and Knipe, 2001; Koledoye et al., 2003). Apart from variable lithologies and throws, other controls on the transmissibility of fluid in fault zones include their 3D geometry, the conditions that led to their formation, the local stress state(s), the arrangement of structures within a fault zone, interactions between fluids and the host rock, and how all these factors vary in space and time (Caine et al., 1996).

Leakage factor calculations indicate two different trends for the interpreted faults. The great majority of faults shows a leakage factor ranging from 0.3 to 0.5, suggesting that sealing units were juxtaposed during faulting and implying a smaller leakage potential (Fig. 15). Juxtaposition diagrams reveal that for F2 and F5, sealing units isolate the intervals units and potentially hinder fluid migration (Fig. 13). A second leakage factor trend for the study area ranges from 0.6 to 0.8, showing a greater potential to leak fluids. The parts of the fault where leakage seems to be occurring coincides with the parts of the fault that are most likely to slip. This constitutes evidence that fault slip is the main mechanism responsible for fluid leakage in a direction parallel to faults (Barton et al., 1995; Wiprut and Zoback, 2000). Largest leakage factors for faults adjacent to D1, D2 and D3 coincide with the fault terminations close to these same salt diapirs. Faults with large leakage factors include the NW-striking crestal faults, faults adjacent to diapirs D2 and D3, and a number of faults in the southern part of the study area (Fig. 15).

Based on our results, we propose that corridors of faults developed around the interpreted salt structures form a preferential pathway for fluids in the study area. Hence, fluid tends to migrate through the faults towards the shallowest diapirs and stratigraphic units (Fig. 16). The preferential fluid pathway in this fault corridor is from south to north-northwest, where the densest accumulation of bright reflections is observed and cross-cut faults developed radially to D3, or above the Salt Ridge (Fig. 16). In such a setting, the combined use of stress analyses and juxtaposition diagrams show that reservoir units within the Espírito Santo Basin are connected through corridors of faults that were developed during the Cretaceous and the Paleogene in association with successive reactivation episodes.

10. Conclusions

This work aimed at understanding if there was a main reactivation style for faults on the continental slope of the Espírito Santo Basin, and how this reactivation controls fluid flow. The main conclusions of this work are summarised as follows:

a) Faults in the study area can be divided into five distinct families according to their location relative to the salt structures. Radial faults occur adjacent to three salt diapirs (D1, D2 and D3), and crestal faults were developed over a NW-trending Salt Ridge. The fifth family of faults occurs in the southern half of the study area, a region that was less affected by halokinesis. The largest faults are NW-trending, whereas the predominant orientations of the smaller faults are NE-SW and E-W.

b) Salt structures evolved in two distinct phases; the first before the Middle Eocene, associated with moderate halokinetic deformation and faulting, and the second after the Middle Eocene recording intense halokinesis. Our observations indicate that the growth of the Salt Ridge was the first to cease in the study area. The growth of diapirs D1 to D3 resulted in the formation of radial faults around them.

c) We found that preferential NE-SW reactivation took place based on the paleostress inversion performed in this work. The inversion results show that the study area was subjected to NNE-SSW extension. Dip-linked reactivation seems to be the preferential reactivation mode for the faults formed in the western part of the study area, contrasting with the eastern part where reactivation by vertical (upward) propagation predominates. Strata younger than the Middle Eocene were barely faulted, except for faults F3 and F7.

d) Slip tendency and leakage factor analysis, combined with juxtaposition diagrams, indicate that the areas most prone to leak fluids occur adjacently to diapirs D1, D2 and D3.

e) Our model proposes that faults are mainly extensional and comprise structural corridors that connect different salt structures. These corridors form a preferential path for fluid flow from south to north-northwest. In such a setting, diapir D3 is the shallowest salt structure in the study area onto which fluid migrates from deeper salt structures to accumulate on its flanks.

Acknowledgements

The authors would like to acknowledge the permission conceded by CGG for the use of the seismic data presented in this paper. The first author would like to acknowledge CAPES (Coordenação de Aperfeiçoamento de Pessoal de Nível Superior – Brazil) for the PhD scholarship under process no. 0877/14-0. Schlumberger (providers of Petrel®), Midland Valley (Move®) and the Southwest Research Institute (3D Stress®) are acknowledged for the provision of the academic licences to Cardiff University 3D Seismic Lab. We thank editor Zheng-Xiang Li, Peter Kukla and an anonymous reviewer for their constructive comments.

References

Ainsworth, R.B., 2006. Sequence stratigraphic-based analysis of reservoir connectivity: influence of sealing faults - a case study from a marginal marine depositional setting. Pet. Geosci. doi:10.1144/1354-079305-661

Allan, U.S., 1989. Model for hydrocarbon migration and entrapment within faulted structures. Am. Assoc. Pet. Geol. Bull. 73, 803–811.

Alves, T.M., 2012. Scale-relationships and geometry of normal faults reactivated during gravitational gliding of Albian rafts (Espírito Santo Basin, SE Brazil). Earth Planet. Sci. Lett. 331, 80–96.

Alves, T.M., Cartwright, J., Davies, R.J., 2009. Faulting of salt-withdrawal basins during early halokinesis: effects on the Paleogene Rio Doce Canyon system (Espírito Santo Basin, Brazil). Am. Assoc. Pet. Geol. Bull. 93, 617–652.

Bailey, W.R., Manzocchi, T., Walsh, J.J., Keogh, K., Hodgetts, D., Rippon, J., Nell, P.A.R., Flint, S., Strand, J.A., 2002. The effect of faults on the 3D connectivity of reservoir bodies: a case study from the East Pennine Coalfield, UK. Pet. Geosci. 8, 263–277. doi:10.1144/petgeo.8.3.263

Barker, P.F., Buffler, R.T., Gambôa, L.A., 1983. A seismic reflection study of the Rio Grande Rise. Initial Reports Deep Sea Drill. Proj. 72, 499–517.

Barnett, J.A.M., Mortimer, J., Rippon, J.H., Walsh, J.J., Watterson, J., 1987. Displacement geometry in the volume containing a single normal fault. Am. Assoc. Pet. Geol. Bull. 71, 925–937.

Barton, C.A., Zoback, M.D., Moos, D., 1995. Fluid flow along potentially active faults in crystalline rock. Geology 23, 683–686.

Baudon, C., Cartwright, J., 2008a. The kinematics of reactivation of normal faults using high resolution throw mapping. J. Struct. Geol. 30, 1072–1084. doi:10.1016/j.jsg.2008.04.008

Baudon, C., Cartwright, J. a., 2008b. 3D seismic characterisation of an array of blind normal faults in the Levant Basin, Eastern Mediterranean. J. Struct. Geol. 30, 746–760. doi:10.1016/j.jsg.2007.12.008

Brown, A.R., 2011. Interpretation of three-dimensional seismic data. American Association of Petroleum Geologists and the Society of Exploration Geophysicists.

Bruhn, C.H.L., Gomes, J.A.T., Del Lucchese Jr, C., Johann, P.R.S., 2003. Campos basin: reservoir characterization and management-Historical overview and future challenges, in: Offshore Technology Conference. Offshore Technology Conference.

Bruhn, C.H.L., Walker, R.G., 1997. Internal architecture and sedimentary evolution of coarse-grained, turbidite channel-levee complexes, Early Eocene Regencia Canyon, Espirito Santo Basin, Brazil. Sedimentology 44, 17–46.

Brun, J.-P., Fort, X., 2011. Salt tectonics at passive margins: Geology versus models. Mar. Pet. Geol. 28, 1123–1145. doi:10.1016/j.marpetgeo.2011.03.004

Caine, J.S., Evans, J.P., Forster, C.B., 1996. Fault zone architechture and permeability structure. Geology 24, 1025–1028. doi:10.1130/0091-7613(1996)024<1025

Cainelli, C., Mohriak, W.U., 1999. Some remarks on the evolution of sedimentary basins along the Eastern Brazilian continental margin. Episodes-Newsmagazine Int. Union Geol. Sci. 22, 206–216.

Cainelli, C., Mohriak, W.U., 1998. Geology of Atlantic eastern Brazilian basins, in: Brazilian Geology

Part. p. 1998.

Carruthers, D., Cartwright, J., Jackson, M.P. a., Schutjens, P., 2013. Origin and timing of layer-bound radial faulting around North Sea salt stocks: New insights into the evolving stress state around rising diapirs. Mar. Pet. Geol. 48, 130–148. doi:10.1016/j.marpetgeo.2013.08.001

Cartwright, J.A., Mansfield, C.S., 1998. Lateral displacement variation and lateral tip geometry of normal faults in the Canyonlands National Park, Utah. J. Struct. Geol. doi:10.1016/S0191-8141(97)00079-5

Chand, S., Mienert, J., Andreassen, K., Knies, J., Plassen, L., Fotland, B., 2008. Gas hydrate stability zone modelling in areas of salt tectonics and pockmarks of the Barents Sea suggests an active hydrocarbon venting system. Mar. Pet. Geol. 25, 625–636. doi:10.1016/j.marpetgeo.2007.10.006

Chang, H.K., Kowsmann, R.O., Figueiredo, A.M.F., Bender, A., 1992. Tectonics and stratigraphy of the East Brazil Rift system: an overview. Tectonophysics 213, 97–138.

Childs, C., Walsh, J.J., Watterson, J., 1997. Complexity in fault zone structure and implications for fault seal prediction. Nor. Pet. Soc. Spec. Publ. 7, 61–72. doi:10.1016/S0928-8937(97)80007-0

Childs, C., Watterson, J., Walsh, J.J., 1995. Fault overlap zones within developing normal fault systems. J. Geol. Soc. London. doi:10.1144/gsjgs.152.3.0535

Cobbold, P.R., Meisling, K.E., Mount, V.S., 2001. Reactivation of an obliquely rifted margin, Campos and Santos basins, southeastern Brazil. Am. Assoc. Pet. Geol. Bull. 85, 1925–1944.

Cowie, P.A., Scholz, C.H., 1992. Physical Explanation for the Displacement Length Relationship of Faults Using a Post-Yield Fracture-Mechanics Model. J. Struct. Geol. 14, 1133–1148.

Cox, S.F., Knackstedt, M.A., Braun, J., 2001. Principles of structural control on permeability and fluid flow in hydrothermal systems. Rev. Econ. Geol. 14, 1–24.

Demercian, S., Szatmari, P., Cobbold, P.R., 1993. Style and pattern of salt diapirs due to thin-skinned gravitational gliding, Campos and Santos basins, offshore Brazil. Tectonophysics 228, 393–433. doi:10.1016/0040-1951(93)90351-J

Diegel, F.A., Karlo, J.F., Schuster, D.C., Shoup, R.C., Tauvers, P.R., 1995. Cenozoic structural evolution and tectono-stratigraphic framework of the northern Gulf Coast continental margin.

Duval, B., Cramez, C., Jackson, M.P. a., 1992. Raft tectonics in the Kwanza Basin, Angola. Mar. Pet. Geol. 9, 389–404. doi:10.1016/0264-8172(92)90050-O

Estrella, G., Mello, M.R., Gaglianone, P.C., Azevedo, R.L.M., Tsubone, K., Rossetti, E., Concha, J., Bruning, I., 1984. The Espirito Santo Basin (Brazil) source rock characterization and petroleum habitat.

Faulkner, D.R., Jackson, C.A.L., Lunn, R.J., Schlische, R.W., Shipton, Z.K., Wibberley, C.A.J., Withjack, M.O., 2010. A review of recent developments concerning the structure, mechanics and fluid flow properties of fault zones. J. Struct. Geol. doi:10.1016/j.jsg.2010.06.009

Ferrill, D.A., Morris, A.P., McGinnis, R.N., 2009. Crossing conjugate normal faults in field exposures and seismic data. Am. Assoc. Pet. Geol. Bull. 93, 1471–1488.

Fiduk, J.C., Brush, E.R., Anderson, L.E., Gibbs, P.B., Rowan, M.G., 2004. Salt deformation, magmatism, and hydrocarbon prospectivity in the Espirito Santo Basin, offshore Brazil, in: Salt-Sediment Interactions and Hydrocarbon Prospectivity: Concepts, Applications, and Case Studies for the 21st Century: Gulf Coast Section SEPM 24th Annual Conference. p. 370.

Fiduk, J.C., Rowan, M.G., 2012. Analysis of folding and deformation within layered evaporites in Blocks BM-S-8 &-9, Santos Basin, Brazil. Geol. Soc. London, Spec. Publ. 363, 471–487.

Figueiredo, A.M.F., Mohriak, W.U., 1984. A tectonica salifera e as acumulacoes de Petroleo da Bacia de Campos, in: Proceedings of the 33rd Brazilian Geological Congress, Sociedada Brasileira de Geologia, Rio de Janeiro. pp. 1380–1394.

Fisher, Q.J., Knipe, R.J., 2001. The permeability of faults within siliciclastic petroleum reservoirs of the North Sea and Norwegian Continental Shelf. Mar. Pet. Geol. 18, 1063–1081.

França, R.L., Del Rey, A.C., Tagliari, C.V., Brandão, J.R., Fontanelli, P. de R., 2007. Bacia do Espírito Santo. Bol. Geociencias da PETROBRAS 15, 501–509.

Frumkin, A., Ezersky, M., Al-Zoubi, A., Akkawi, E., Abueladas, A.-R., 2011. The Dead Sea sinkhole hazard: Geophysical assessment of salt dissolution and collapse. Geomorphology 134, 102–117.

Gamboa, D.A., 2011. An integrated seismic-scale analysis of reservoir compartmentalisation on continental margins: the Espirito Santo Basin, SE Brazil.

Gamboa, D., Alves, T., Cartwright, J., Terrinha, P., 2010. MTD distribution on a “passive” continental margin: The Espírito Santo Basin (SE Brazil) during the Palaeogene. Mar. Pet. Geol. 27, 1311–1324. doi:10.1016/j.marpetgeo.2010.05.008

Gamboa, D., Alves, T.M., 2015. Spatial and dimensional relationships of submarine slope architectural elements: A seismic-scale analysis from the Espírito Santo Basin (SE Brazil). Mar. Pet. Geol. 64, 43–57.

Gamboa, D., Alves, T.M., Cartwright, J., 2012. A submarine channel confluence classification for topographically confined slopes. Mar. Pet. Geol. 35, 176–189. doi:10.1016/j.marpetgeo.2012.02.011

Gartrell, A., Zhang, Y., Lisk, M., Dewhurst, D., 2004. Fault intersections as critical hydrocarbon leakage zones: integrated field study and numerical modelling of an example from the Timor Sea, Australia. Mar. Pet. Geol. 21, 1165–1179. doi:10.1016/j.marpetgeo.2004.08.001

Gartrell, A., Zhang, Y., Lisk, M., Dewhurst, D., 2003. Enhanced hydrocarbon leakage at fault intersections: an example from the Timor Sea, Northwest Shelf, Australia. J. Geochemical Explor. 78, 361–365.

Ge, H., Jackson, M.P.A., 1998. Physical modeling of structures formed by salt withdrawal: Implications for deformation caused by salt dissolution. Am. Assoc. Pet. Geol. Bull. 82, 228–250.

Guardado, L.R., Spadini, A.R., Brandão, J.S.L., Mello, M.R., 2000. Petroleum System of the Campos

Basin, Brazil. AAPG Mem. 73.

Guerra, M.C.M., Underhill, J.R., 2012. Role of halokinesis in controlling structural styles and sediment dispersal in the Santos Basin, offshore Brazil. Geol. Soc. London, Spec. Publ. 363, 175–206.

Henriksen, E., Ryseth, A.E., Larssen, G.B., Heide, T., Ronning, K., Sollid, K., Stoupakova, A. V., 2011. Tectonostratigraphy of the greater Barents Sea: implications for petroleum systems. Geol. Soc. London, Mem. doi:10.1144/M35.10

Hudec, M.R., Jackson, M.P.A., 2002. Structural segmentation, inversion, and salt tectonics on a passive margin: Evolution of the Inner Kwanza Basin, Angola. Geol. Soc. Am. Bull. 114, 1222–1244.

Hudec, M.R., Jackson, M.P. a., 2007. Terra infirma: Understanding salt tectonics. Earth-Science Rev. 82, 1–28. doi:10.1016/j.earscirev.2007.01.001

Jackson, M.P.A., Vendeville, B.C., Schultz-Ela, D.D., 1994. Structural Dynamics of Salt Systems. Annu. Rev. Earth Planet. Sci. 22, 93–117. doi:10.1146/annurev.ea.22.050194.000521

Jolley, S.J., Barr, D., Walsh, J.J., Knipe, R.J., 2007. Structurally complex reservoirs: an introduction. Geol. Soc. London, Spec. Publ. 292, 1–24.

Jolley, S.J., Fisher, Q.J., Ainsworth, R.B., 2010. Reservoir compartmentalization: an introduction. Geol. Soc. London, Spec. Publ. 347, 1–8. doi:10.1144/SP347.1

Jones, R.M., Hillis, R.R., 2003. An integrated, quantitative approach to assessing fault-seal risk. Am. Assoc. Pet. Geol. Bull. 87, 507–524.

Kane, K.E., Jackson, C. a.-L., Larsen, E., 2010. Normal fault growth and fault-related folding in a salt-influenced rift basin: South Viking Graben, offshore Norway. J. Struct. Geol. 32, 490–506. doi:10.1016/j.jsg.2010.02.005

Katz, B.J., Mello, M.R., 2000. Petroleum Systems of South Atlantic Marginal Basins - An Overview. AAPG Mem. 73.

Kelly, P.G., Peacock, D.C.P., Sanderson, D.J., McGurk, A.C., 1999. Selective reverse-reactivation of normal faults, and deformation around reverse-reactivated faults in the Mesozoic of the Somerset coast. J. Struct. Geol. 21, 493–509. doi:10.1016/S0191-8141(99)00041-3

Knipe, R.J., 1997. Juxtaposition and seal diagrams to help analyze fault seals in hydrocarbon reservoirs. Am. Assoc. Pet. Geol. Bull. 81, 187–195. doi:10.1306/522B42DF-1727-11D7-8645000102C1865D

Knipe, R.J., Jones, G., Fisher, Q.J., 1998. Faulting, fault sealing and fluid flow in hydrocarbon reservoirs: an introduction. Geol. Soc. London, Spec. Publ. doi:10.1144/GSL.SP.1998.147.01.01

Koledoye, B.A., Aydin, A., May, E., 2003. A new process-based methodology for analysis of shale smear along normal faults in the Niger Delta. Am. Assoc. Pet. Geol. Bull. 87, 445–463.

Koyi, H., Talbot, C.J., Tørudbakken, B.O., 1993. Salt diapirs of the southwest Nordkapp Basin: analogue modelling. Tectonophysics 228, 167–187.

Lima, C., Nascimento, E., Assumpção, M., 1997. Stress orientations in Brazilian sedimentary basins from breakout analysis: implications for force models in the South American plate. Geophys. J. Int. 130, 112–124.

Lohr, T., Krawczyk, C.M., Tanner, D.C., Samiee, R., Endres, H., Thierer, P.O., Oncken, O., Trappe, H., Bachmann, R., Kukla, P.A., 2008. Prediction of subseismic faults and fractures: Integration of three-dimensional seismic data, three-dimensional retrodeformation, and well data on an example of deformation around an inverted fault. Am. Assoc. Pet. Geol. Bull. 92, 473–485.

Mansfield, C.S., Cartwright, J.A., 1996. High resolution fault displacement mapping from three-dimensional seismic data: evidence for dip linkage during fault growth. J. Struct. Geol. 18, 249–263. doi:10.1016/S0191-8141(96)80048-4

Manzocchi, T., Childs, C., Walsh, J.J., 2010. Faults and fault properties in hydrocarbon flow models. Geofluids 10, 94–113.

Mattos, N.H., Alves, T.M., Omosanya, K.O., 2016. Crestal fault geometries reveal late halokinesis and collapse of the Samson Dome, Northern Norway: Implications for petroleum systems in the Barents Sea. Tectonophysics.

McFarland, J.M., Morris, A.P., Ferrill, D.A., 2012. Stress inversion using slip tendency. Comput. Geosci. 41, 40–46.

Meisling, K.E., Cobbold, P.R., Mount, V.S., 2001. Segmentation of an obliquely rifted margin, Campos and Santos basins, southeastern Brazil. Am. Assoc. Pet. Geol. Bull. 85, 1903–1924.

Milani, E.J., Brandão, J.A.S.L., Zalán, P. V., Gamboa, L.A.P., 2001. Petróleo na Margem Continental Brasileira: Geologia, exploração, resultados e perspectivas. Brazilian J. Geophys. 18, 351–396.

Mohriak, W.U., 2005. Interpretação geológica e geofísica da Bacia do Espírito Santo e da região de Abrolhos: petrografia, datações radiométricas e visualização sísmica das rochas vulcânicas. Bol. Geoc. Petrobrás 14, 133–142.

Mohriak, W.U., 2003. Bacias sedimentares da margem continental Brasileira. Geol. Tectônica e Recur. Minerais do Bras. 87–165.

Mohriak, W.U., Nemčok, M., Enciso, G., 2008. South Atlantic divergent margin evolution: rift-border uplift and salt tectonics in the basins of SE Brazil. Geol. Soc. London, Spec. Publ. 294, 365–398.

Moraes, M.A.S., Maciel, W.B., Braga, M.S.S., Viana, A.R., 2007. Bottom-current reworked Palaeocene-Eocene deep-water reservoirs of the Campos Basin, Brazil. Geol. Soc. London, Spec. Publ. 276, 81–94.

Morley, C.K., Guerin, G., 1996. Comparison of gravity-driven deformation styles and behavior associated with mobile shales and salt. Tectonics 15, 1154–1170.

Morris, A., Ferrill, D. a, Henderson, D.B., 1996. Slip-tendency analysis and fault reactivation. Geology 24, 275–278. doi:10.1130/0091-7613(1996)024<0275

Muraoka, H., Kamata, H., 1983. Displacement distribution along minor fault traces. J. Struct. Geol. 5, 483–495. doi:10.1016/0191-8141(83)90054-8

Nicol, A., Gillespie, P.A., Childs, C., Walsh, J.J., 2002. Relay zones between mesoscopic thrust faults in layered sedimentary sequences. J. Struct. Geol. 24, 709–727.

Nicol, A., Watterson, J., Walsh, J.J., Childs, C., 1996. The shapes, major axis orientations and displacement patterns of fault surfaces. J. Struct. Geol. doi:10.1016/S0191-8141(96)80047-2

Ojeda, H.A.O., 1982. Structural framework, stratigraphy, and evolution of Brazilian marginal basins. Am. Assoc. Pet. Geol. Bull. 66, 732–749.

Omosanya, K.O., Alves, T.M., 2014. Mass-transport deposits controlling fault propagation, reactivation and structural decoupling on continental margins (Espírito Santo Basin, SE Brazil). Tectonophysics 628, 158–171. doi:http://dx.doi.org/10.1016/j.tecto.2014.04.045

Omosanya, K.O., Alves, T.M., 2013. A 3-dimensional seismic method to assess the provenance of Mass-Transport Deposits (MTDs) on salt-rich continental slopes (Espírito Santo Basin, SE Brazil). Mar. Pet. Geol. 44, 223–239. doi:10.1016/j.marpetgeo.2013.02.006

Omosanya, K.O., Johansen, S.E., Harishidayat, D., 2015. Evolution and character of supra-salt faults in the Easternmost Hammerfest Basin, SW Barents Sea. Mar. Pet. Geol.

Peacock, D.C.P., Sanderson, D.J., 1996. Effects of propagation rate on displacement variations along faults. J. Struct. Geol. 18, 311–320.

Peacock, D.C.P., Sanderson, D.J., 1991. Displacements, segment linkage and relay ramps in normal fault zones. J. Struct. Geol. 13, 721–733. doi:10.1016/0191-8141(91)90033-F

Quirk, D.G., Schødt, N., Lassen, B., Ings, S.J., Hsu, D., Hirsch, K.K., Von Nicolai, C., 2012. Salt tectonics on passive margins: examples from Santos, Campos and Kwanza basins. Geol. Soc. London, Spec. Publ. 363, 207–244.

Reilly, C., Nicol, A., Walsh, J.J., Kroeger, K.F., 2016. Temporal changes of fault seal and early charge of the Maui Gas-condensate field, Taranaki Basin, New Zealand. Mar. Pet. Geol. 70, 237–250.

Rowan, M.G., Jackson, M.P.A., Trudgill, B.D., 1999. Salt-related fault families and fault welds in the northern Gulf of Mexico. Am. Assoc. Pet. Geol. Bull. doi:10.1306/E4FD41E3-1732-11D7-8645000102C1865D

Scholz, C.H., Cowie, P.A., 1990. Determination of total strain from faulting using slip measurements.

Seni, S.J., Jackson, M.P.A., 1984. Sedimentary Record of Cretaceous and Tertiary Salt Movement, East Texas Basin: Times, Rates, and Volumes of Salt Flow and Their Implications for Nuclear Waste Isolation and Petroleum Exploration. Bureau of Economic Geology, University of Texas of Austin.

Sheriff, R.E., Geldart, L.P., 1995. Exploration Seismology, Second Edi. ed. Cambridge University Press, Cambridge. doi:10.1017/CBO9781139168359

Sibson, R.H., 1996. Structural permeability of fluid-driven fault-fracture meshes. J. Struct. Geol. 18, 1031–1042.

Smit, J., Brun, J.-P., Fort, X., Cloetingh, S., Ben-Avraham, Z., 2008. Salt tectonics in pull-apart basins with application to the Dead Sea Basin. Tectonophysics 449, 1–16. doi:10.1016/j.tecto.2007.12.004

Stewart, S. a., 2006. Implications of passive salt diapir kinematics for reservoir segmentation by radial and concentric faults. Mar. Pet. Geol. 23, 843–853. doi:10.1016/j.marpetgeo.2006.04.001

Strozyk, F., Back, S., Kukla, P.A., 2017. Comparison of the rift and post-rift architecture of conjugated salt and salt-free basins offshore Brazil and Angola/Namibia, South Atlantic. Tectonophysics 716, 204-224. doi:10.1016/j.tecto.2016.12.012.

Talbot, C., Rönnlund, P., Schmeling, H., 1991. Diapiric spoke patterns. Tectonophysics 188, 187–201.

Talbot, C.J., 1993. Spreading of salt structures in the Gulf of Mexico. Tectonophysics 228, 151–166. doi:10.1016/0040-1951(93)90338-K

Varela, C.L., Mohriak, W.U., 2013. Halokinetic rotating faults, salt intrusions, and seismic pitfalls in the petroleum exploration of divergent margins. Am. Assoc. Pet. Geol. Bull. doi:10.1306/02261312164

Vendeville, B.C., 2002. A new interpretation of Trusheim's classic model of salt-diapir growth.

Vendeville, B.C., Jackson, M.P. a., 1992. The rise of diapirs during thin-skinned extension. Mar. Pet. Geol. 9, 331–354. doi:10.1016/0264-8172(92)90047-I

Viana, A., Figueiredo, A., Faugres, J.-C., Lima, A., Gonthier, E., Brehme, I., Zaragosi, S., 2003. The São Tomé deep-sea turbidite system (southern Brazil Basin): Cenozoic seismic stratigraphy and sedimentary processes. Am. Assoc. Pet. Geol. Bull. 87, 873–894.

Vieira, R.A.B., Mendes, M.P., Vieira, P.E., Costa, L.A.R., Tagliari, C. V, Bacelar, L.A.P., Feijó, F.J., 1994. Bacias do Espírito Santo e Mucuri. Bol. Geosci. da Petrobrás, Rio Janeiro 8, 191–202.

Walsh, J.J., Bailey, W.R., Childs, C., Nicol, A., Bonson, C.G., 2003. Formation of segmented normal faults: a 3-D perspective. J. Struct. Geol. 25, 1251–1262.

Walsh, J.J., Nicol, A., Childs, C., 2002. An alternative model for the growth of faults. J. Struct. Geol. 24, 1669–1675. doi:10.1016/S0191-8141(01)00165-1

Walsh, J.J., Watterson, J., 1989. Displacement gradients on fault surfaces. J. Struct. Geol. doi:10.1016/0191-8141(89)90070-9

Walsh, J.J., Watterson, J., 1987. Distributions of cumulative displacement and seismic slip on a single normal fault surface. J. Struct. Geol. doi:10.1016/0191-8141(87)90012-5

Walsh, J.J., Watterson, J., Heath, A.E., Childs, C., 1998. Representation and scaling of faults in fluid flow models. Pet. Geosci. doi:10.1144/petgeo.4.3.241

Wiprut, D., Zoback, M.D., 2000. Fault reactivation and fluid flow along a previously dormant normal fault in the northern North Sea. Geology 28, 595–598.

Ze, T., Alves, T.M., 2016. The role of gravitational collapse in controlling the evolution of crestal fault systems (Espírito Santo Basin, SE Brazil). J. Struct. Geol. 92, 79–98.

Zoback, M.D., 2010. Reservoir geomechanics. Cambridge University Press.

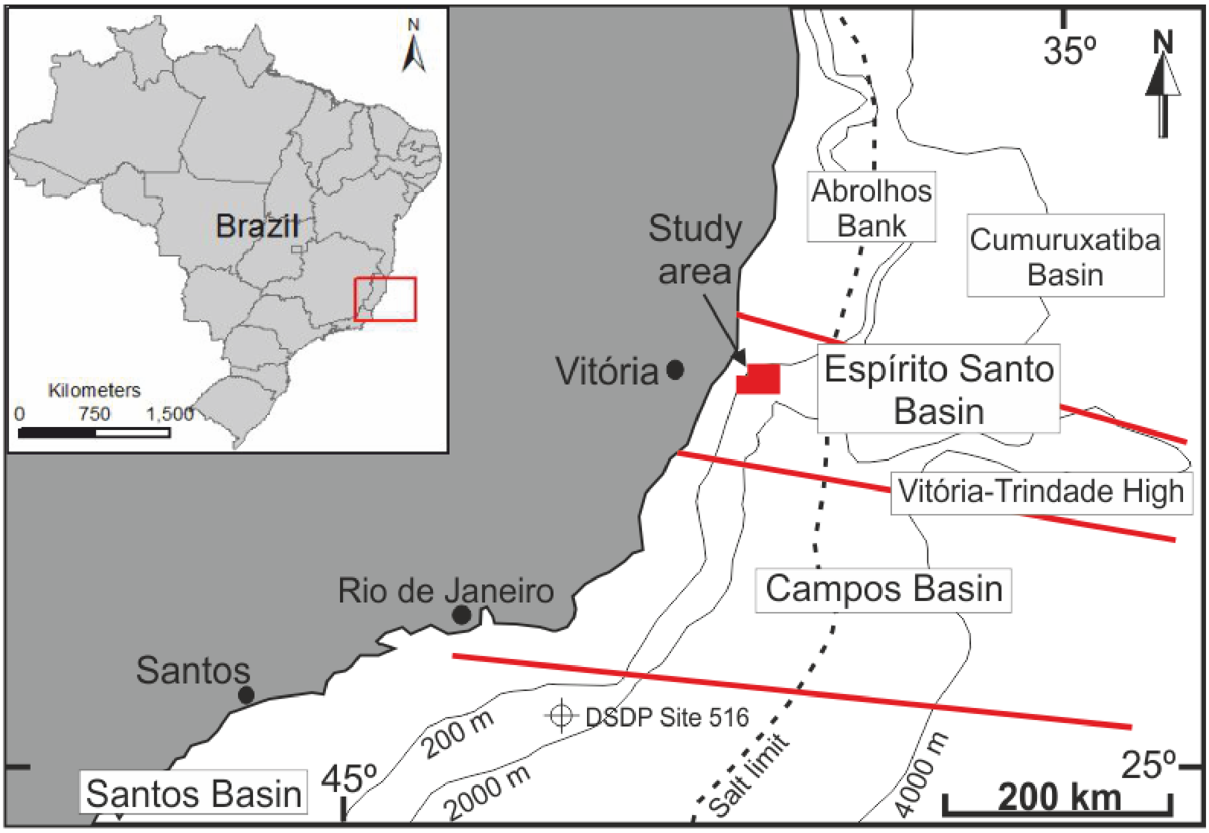

Figure 1: Location map of the Espírito Santo Basin and its main boundaries. The Espírito Santo Basin is limited to the north by the Abrolhos Bank and to the south by the Vitória-Trindade High. The location of the 3D seismic cube is indicated by the red polygon.

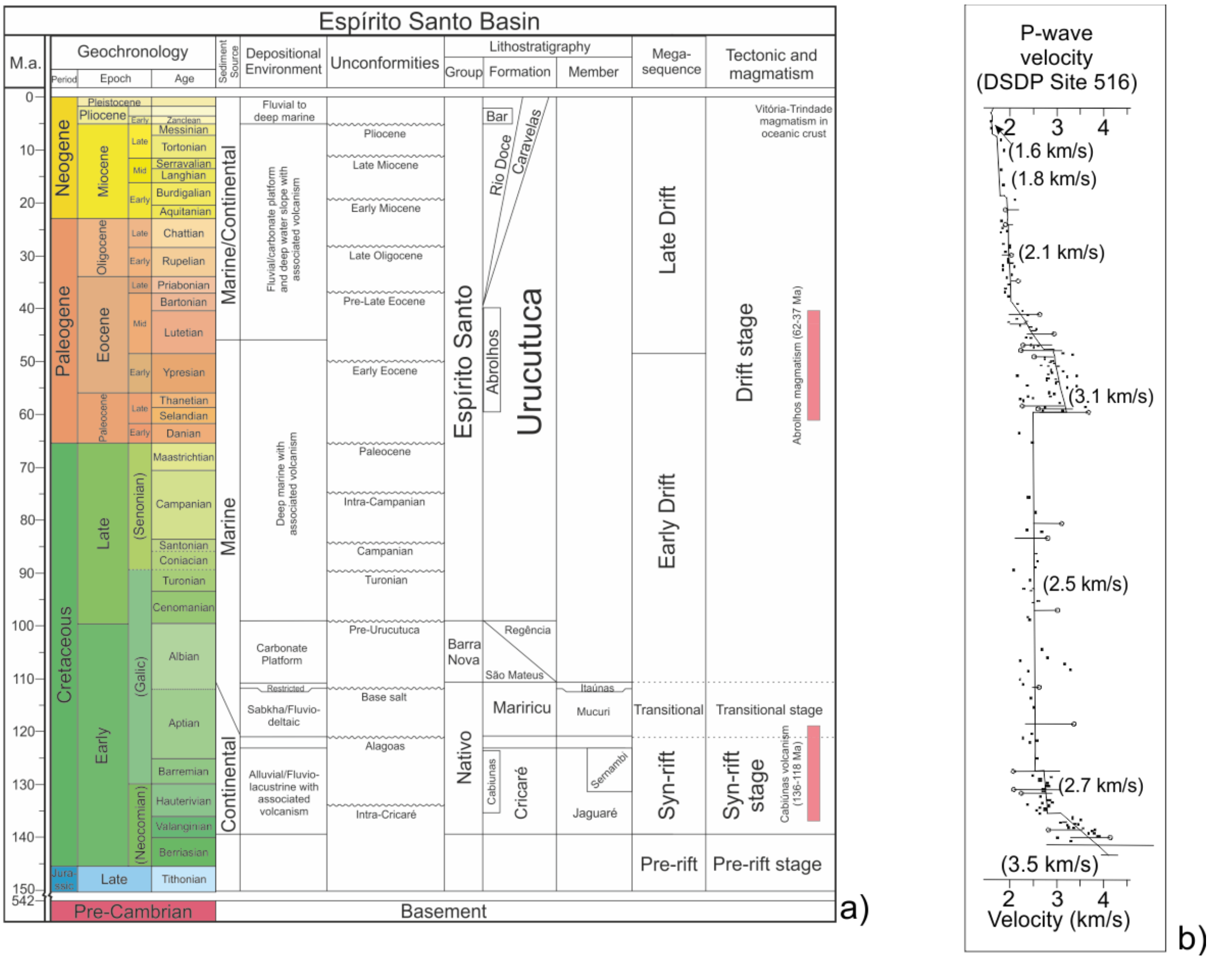

Figure 2: Stratigraphic column of the Espírito Santo Basin highlighting main sediment sources and depositional environments. Four tectonic stages and five depositional megasequences are documented in the basin (Modified from França et al., 2007).Velocity data for well DSDP Site 516 for the Rio Grande Rise compiled from Barker et al. (1983).

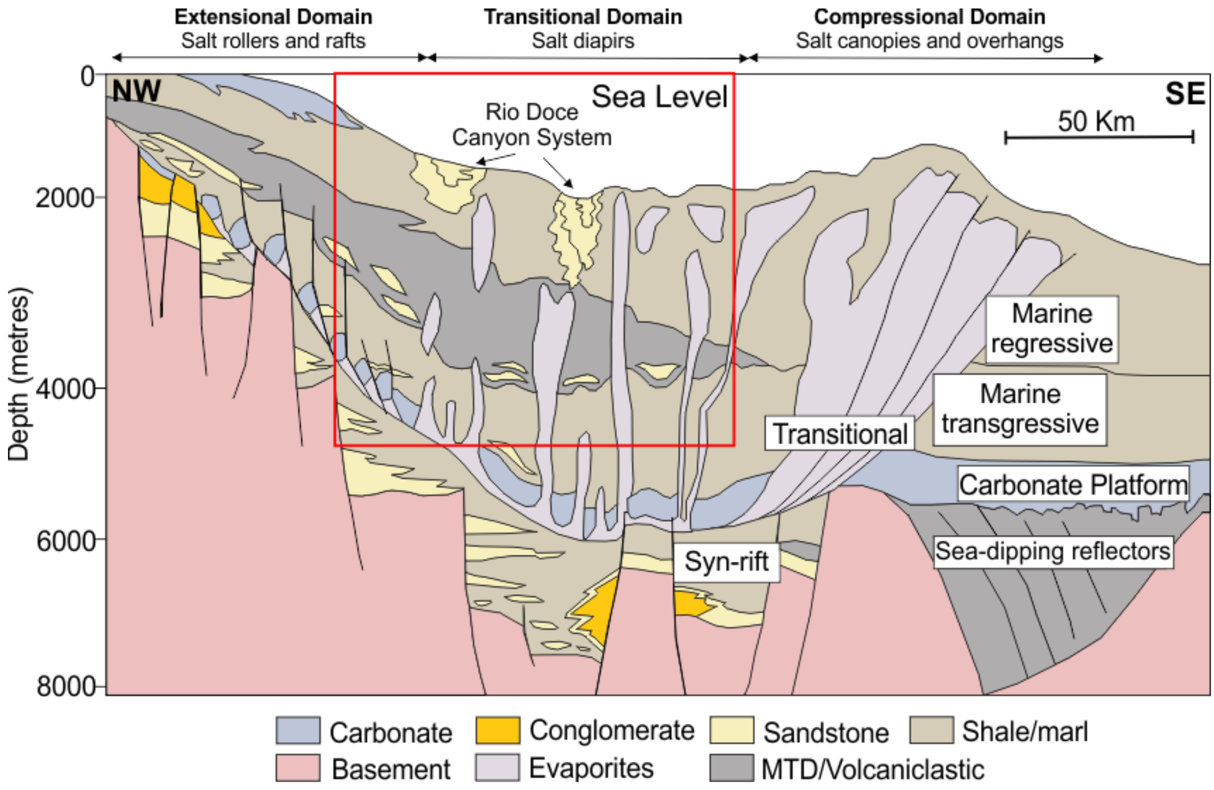

Figure 3: Simplified regional section of the Espírito Santo Basin showing major depositional sequences and salt structures across three structural domains: extensional, transitional and compressional. The approximate location of the study area is shown by the red polygon, within the extensional and transitional domains. Modified from Fiduk et al. (2004) and Gamboa (2011).

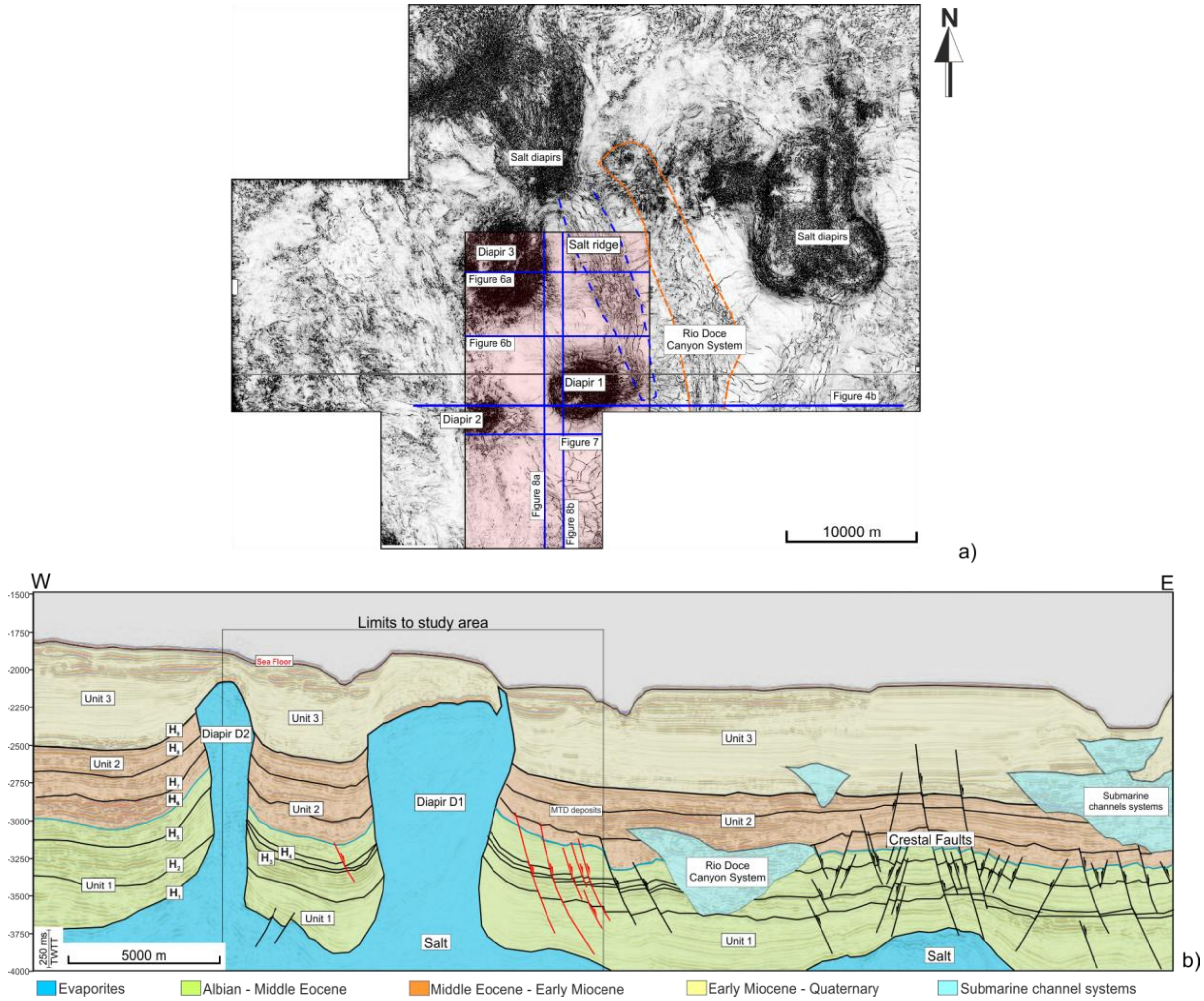

Figure 4: a) Variance time-slice at -3250 ms showing main geological features in the block BES-2. Salt diapirs and ridges are distinctive structures in this seismic cube. The Rio Doce Canyon System is delimited by the orange dashed line. The area of interest of this study is delimited by the red polygon. Three radially faulted salt diapirs and a faulted salt ridge are observed in the variance map. A large number of faults occur toward the southern half of the red polygon. b) Interpreted W-E regional seismic section of the Espírito Santo Basin showing main structures in the study area. The black polygon delimits the area of interest of this study and the faults adjacent to Diapir 2 are indicated in red. The blue line represents the Mid-Eocene unconformity (horizon H_6).

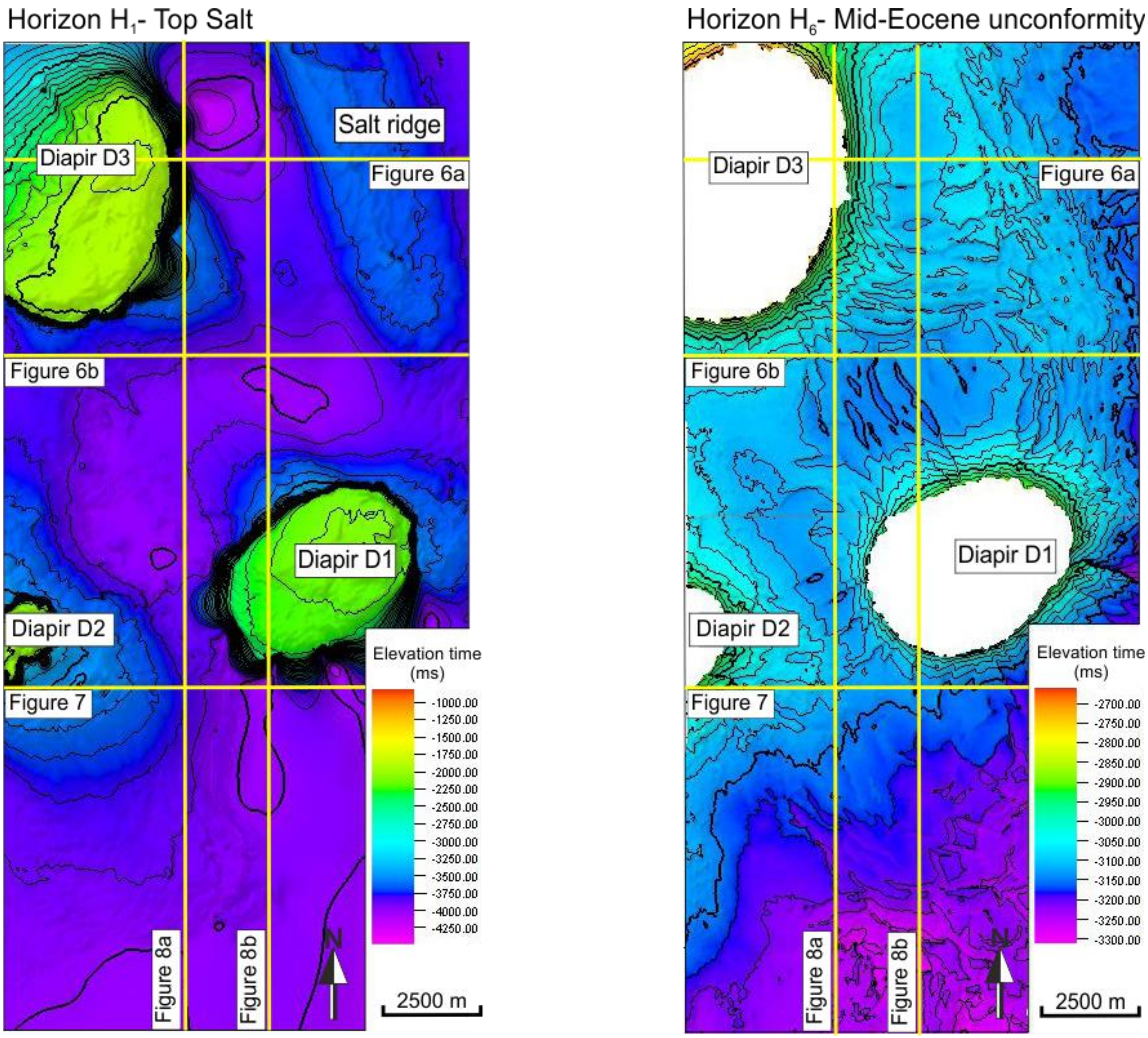

Figure 5: a) TWTT structural map of horizon H_1 highlighting the occurrence of salt diapirs and ridge in the study area. b) TWTT structural map of the regional Mid-Eocene unconformity (horizon H_6). Radial faults are observed adjacently to diapirs D2 and D3. However, these faults rarely propagate into Unit 2, which is delimited by horizon H_6 at its base.

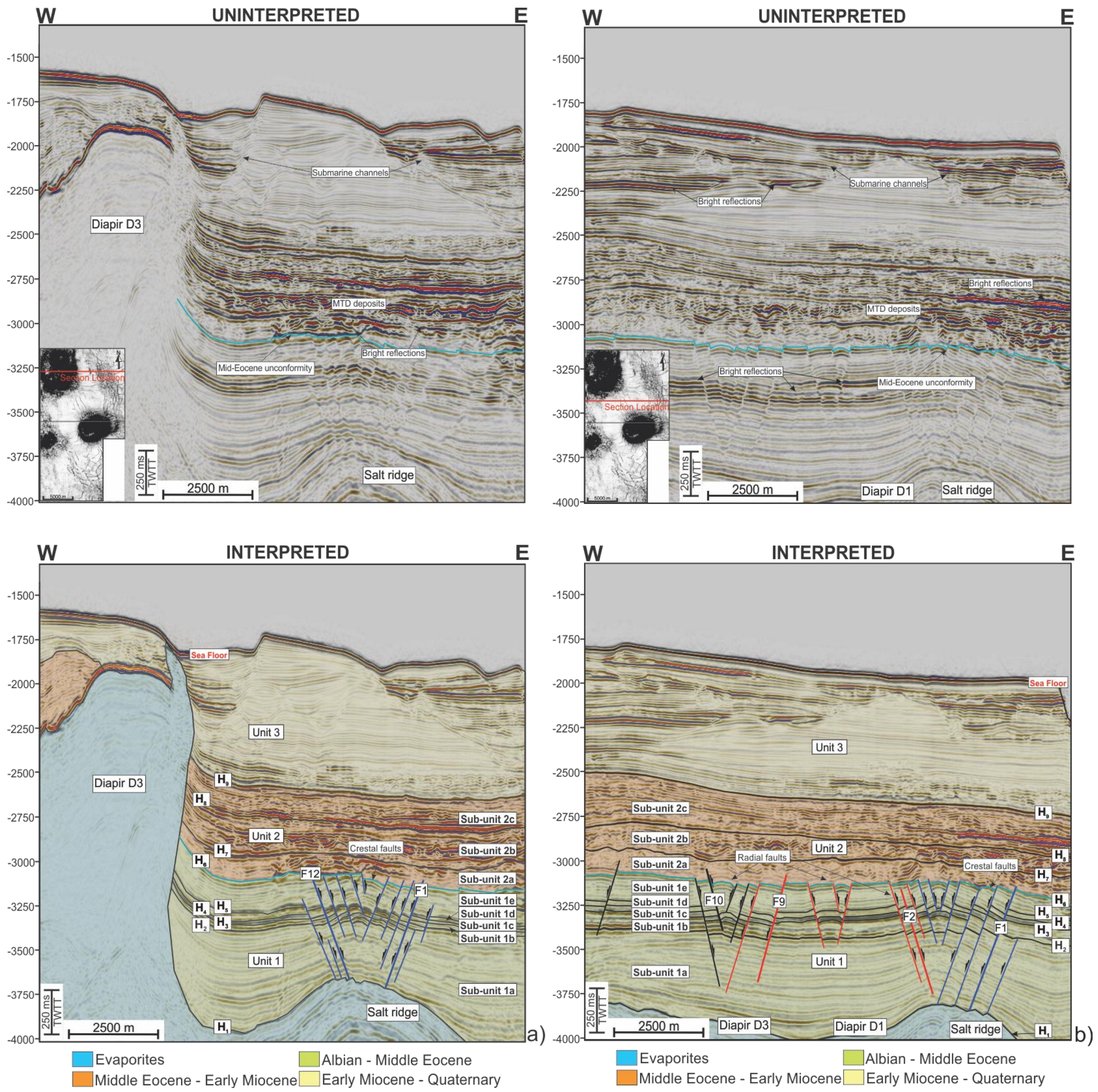

Figure 6: Sets of uninterpreted and interpreted W-E seismic sections. a) Seismic section crossing Diapir D3 and the Salt Ridge. Submarine channels are observed close to the seafloor and characterised by bright reflections. The interpreted seismic section highlights the presence of faults F1 and F12. Faults at the crest of the Salt Ridge comprise tilt blocks and terminate at horizon H_6, around which bright reflections are observed. Strata from Units 1 to 3 are deformed adjacent to diapir D3. b) Seismic section located between the salt structures highlighting the occurrence of bright reflections adjacent to D1 and D3 and the Salt Ridge. The interpreted seismic section shows that faults adjacent to D1 form tilt blocks with faults from the Salt Ridge and D3. Faults from D1 and D3 propagates into sub-unit 2a, whereas faults propagating from the Salt Ridge terminate at horizon H_6. Representative faults observed in this section include F1, F2, F9 and F10. The blue line represents the Mid-Eocene unconformity (horizon H_6).

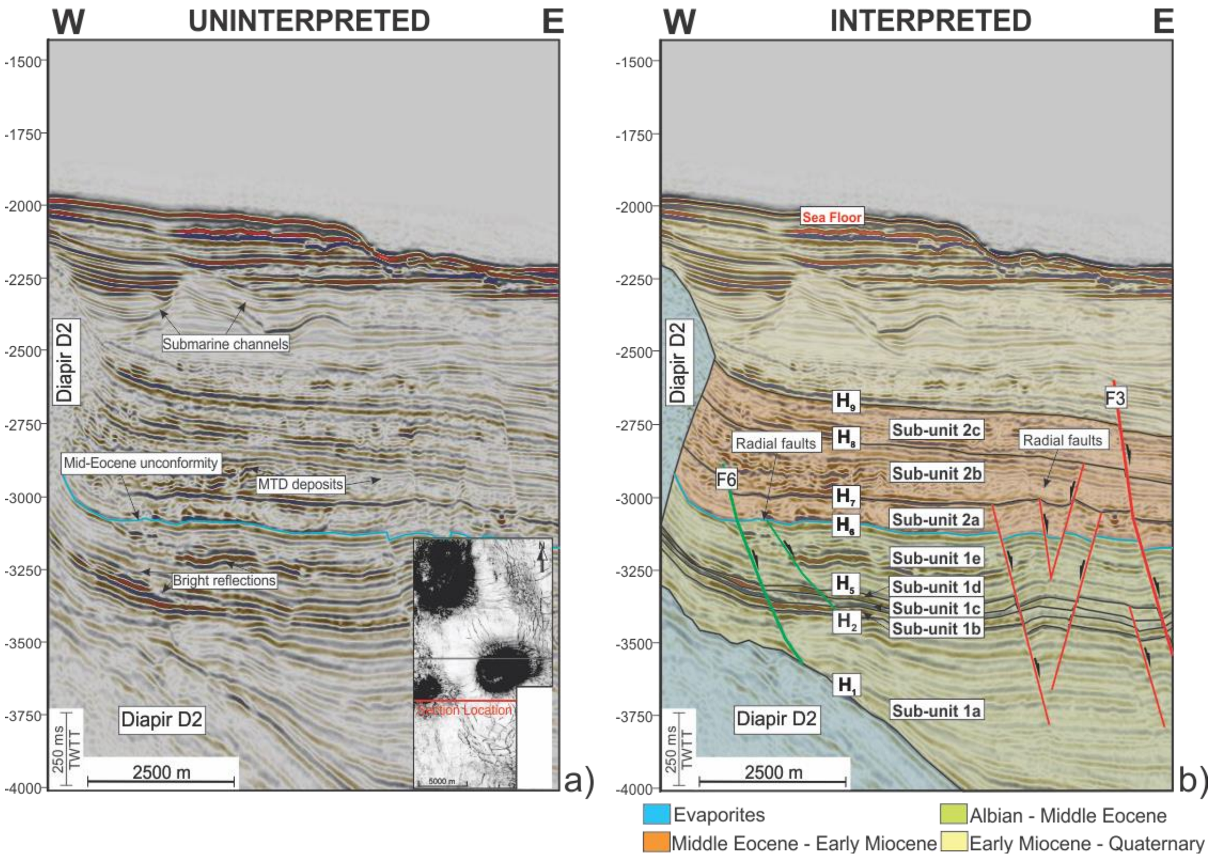

Figure 7: a) Uninterpreted W-E seismic line in the Espírito Santo Basin highlighting the occurrence of bright reflections close to diapir D2. Submarine channels are observed at a depth of -2500 ms below the sea floor. b) Interpreted seismic section showing that D2 deforms the three stratigraphic units. Representative faults in this region include faults F3 and F6. Fault F3 offsets Units 1 to 3, whereas fault F6 offsets Units 1 and 2. The blue line represents the Mid-Eocene unconformity (horizon H_6).

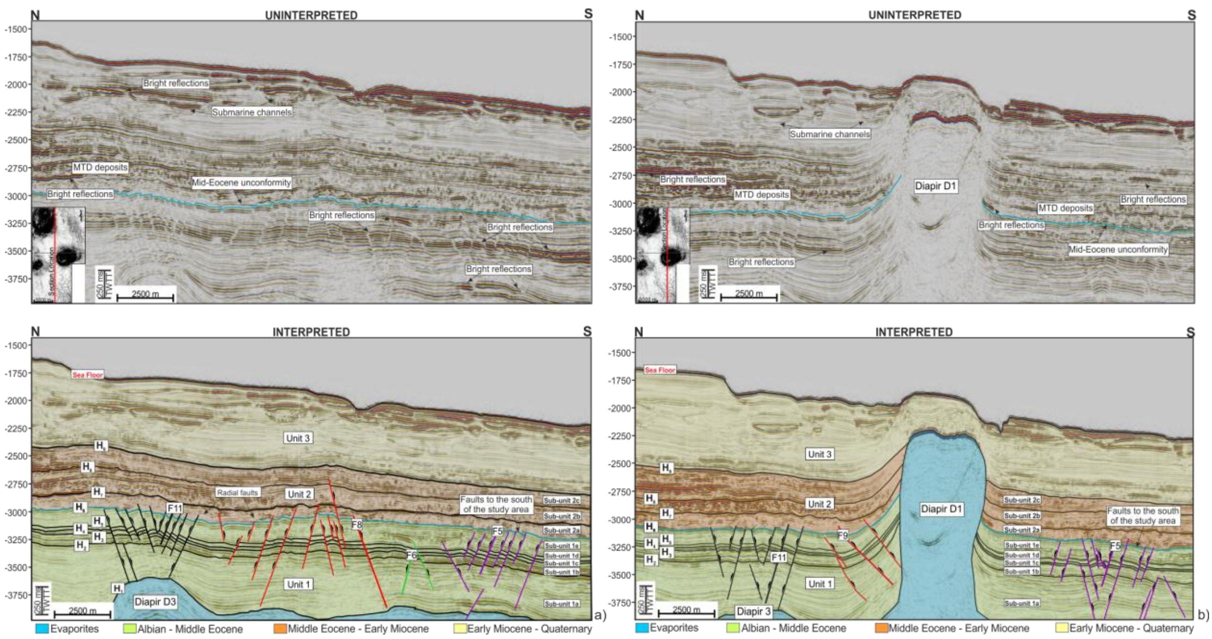

Figure 8: Uninterpreted and interpreted N-S seismic sections across the study area. a) Seismic section showing faults adjacent to diapirs D1, D2 and D3, and faults to the south of the study area. Bright reflections occur close to the sea floor, in Unit 2 to the north and in sub-units 1a to 1c for faults adjacent to D1 and D2 and to the south Faults adjacent to D1 and D3 offset Unit 2, whereas faults to the south are restricted to Unit 1. Representative faults observed in this section include F5, F6, F8 and F11. b) Seismic section showing that strata are deformed in the proximities of D1, and the radial character of the faults. Faults related to D3 and faults in the Southern Area form tilt blocks to the north and the south of this section, respectively. Representative faults observed in this section include F5, F9 and F11. The blue line represents the Mid-Eocene unconformity (horizon H_6).

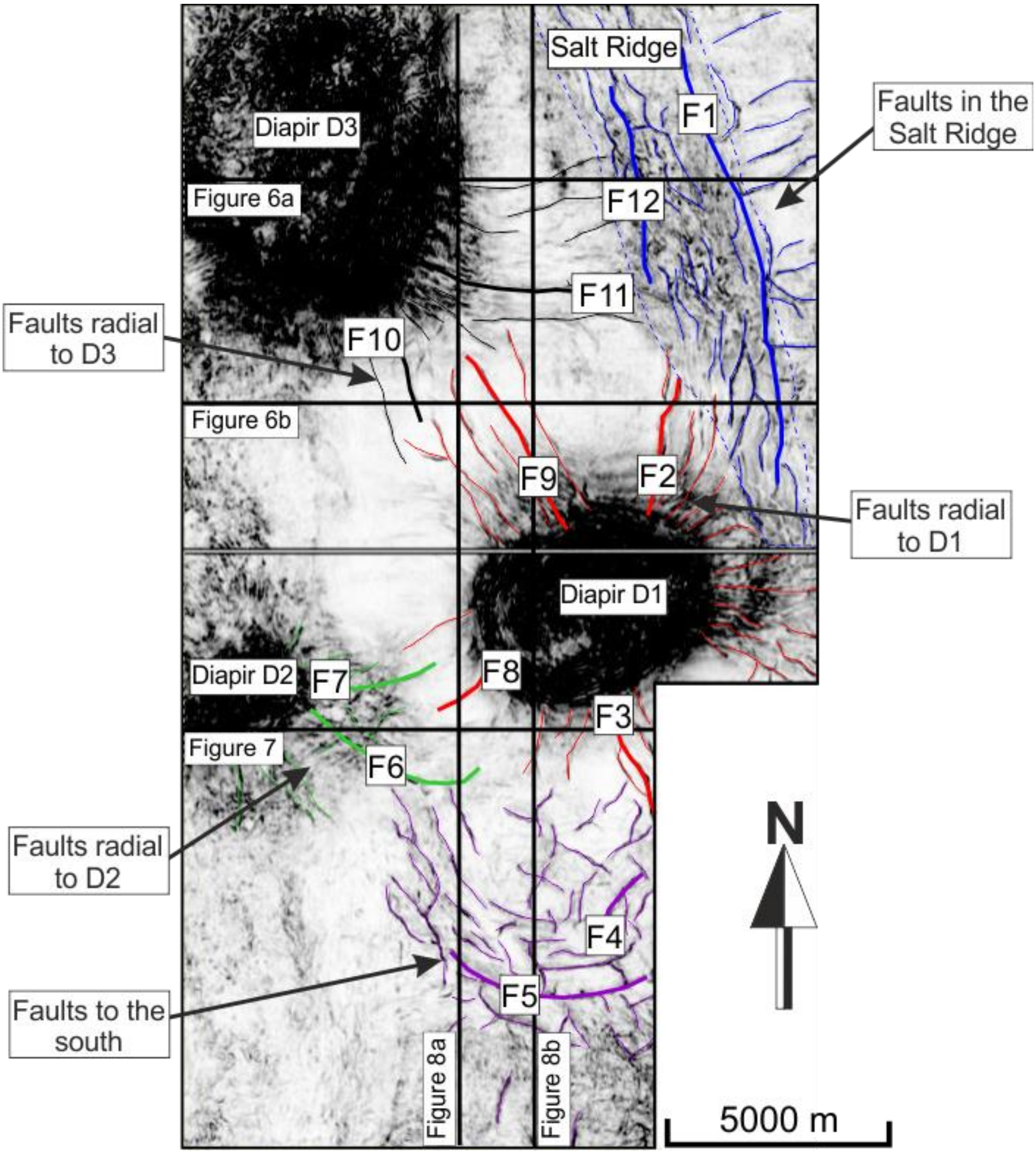

Figure 9: Variance time-slice at -3500 ms showing the locations of main fault families interpreted in the study area. Faults associated with the Salt Ridge are represented by the colour blue, whereas faults adjacent to D1 are in red. Faults to the south of the study area and adjacent to diapirs D2 and D3 are respectively shown in purple, green and black colours.

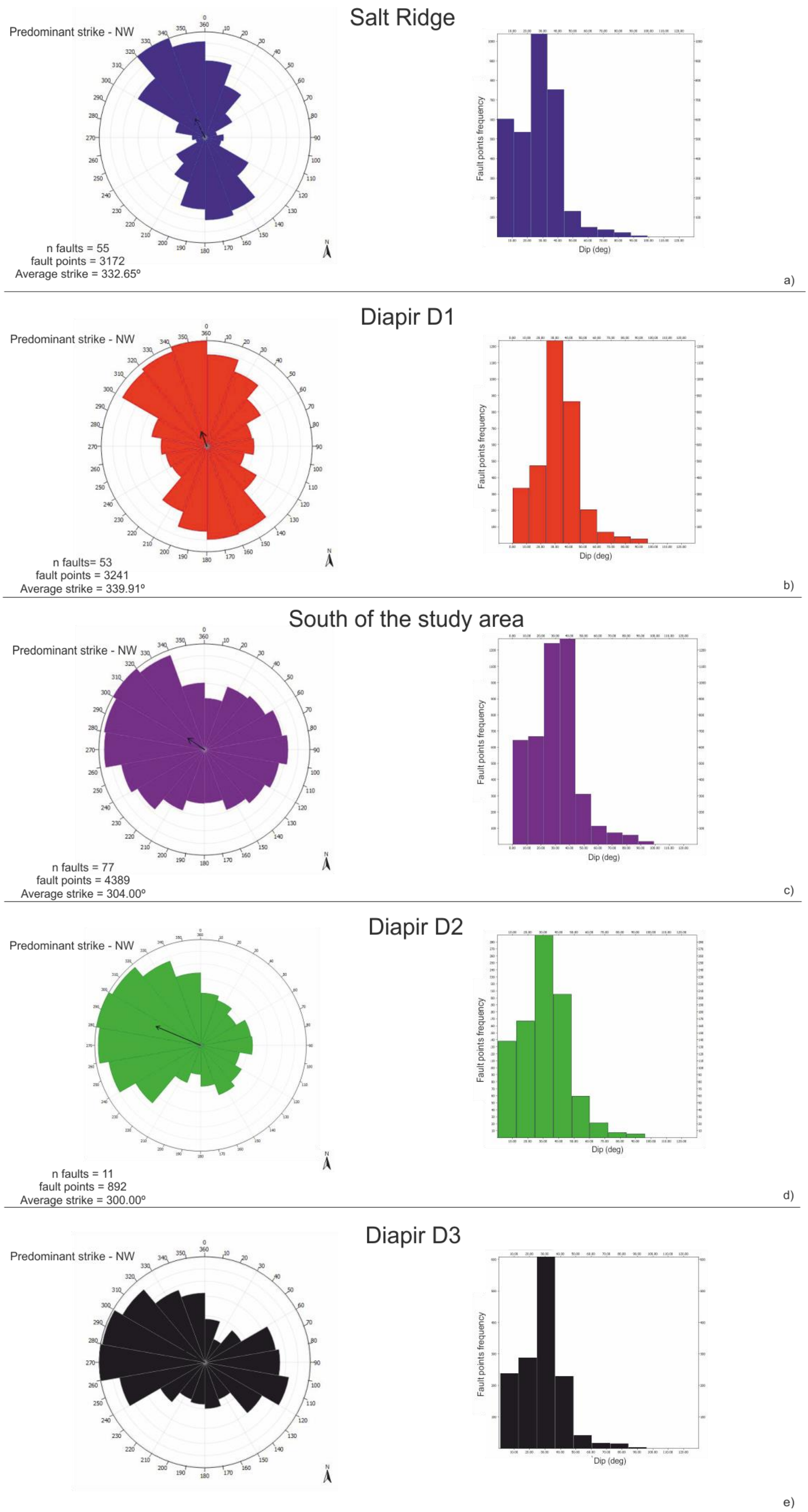
Salt Ridge
Predominant strike - NW
n faults = 55
fault points = 3172
Average strike = 332.65º
Fault points frequency
Dip (deg)
a)
Diapir D1
Predominant strike - NW
n faults= 53
fault points = 3241
Average strike = 339.91º
Fault points frequency
Dip (deg)
b)
South of the study area
Predominant strike - NW
n faults = 77
fault points = 4389
Average strike = 304.00º
Fault points frequency
Dip (deg)
c)
Diapir D2
Predominant strike - NW
n faults = 11
fault points = 892
Average strike = 300.00º
Fault points frequency
Dip (deg)
d)
Diapir D3
Predominant strike - NW
Fault points frequency
Dip (deg)
e)

Figure 10: Rose diagrams showing the strike and histograms showing the dip magnitude for the faults in the study area. Predominant strikes for the Salt Ridge are NW-SE and NE-SW. Faults close to D1 trend preferentially towards NW and NNE. In the south of the study area, faults are predominantly NW-SE and E-W. Faults predominantly strike to NW and SW close to D2. In diapir D3, faults show a predominant NW strike and a secondary SW strike.

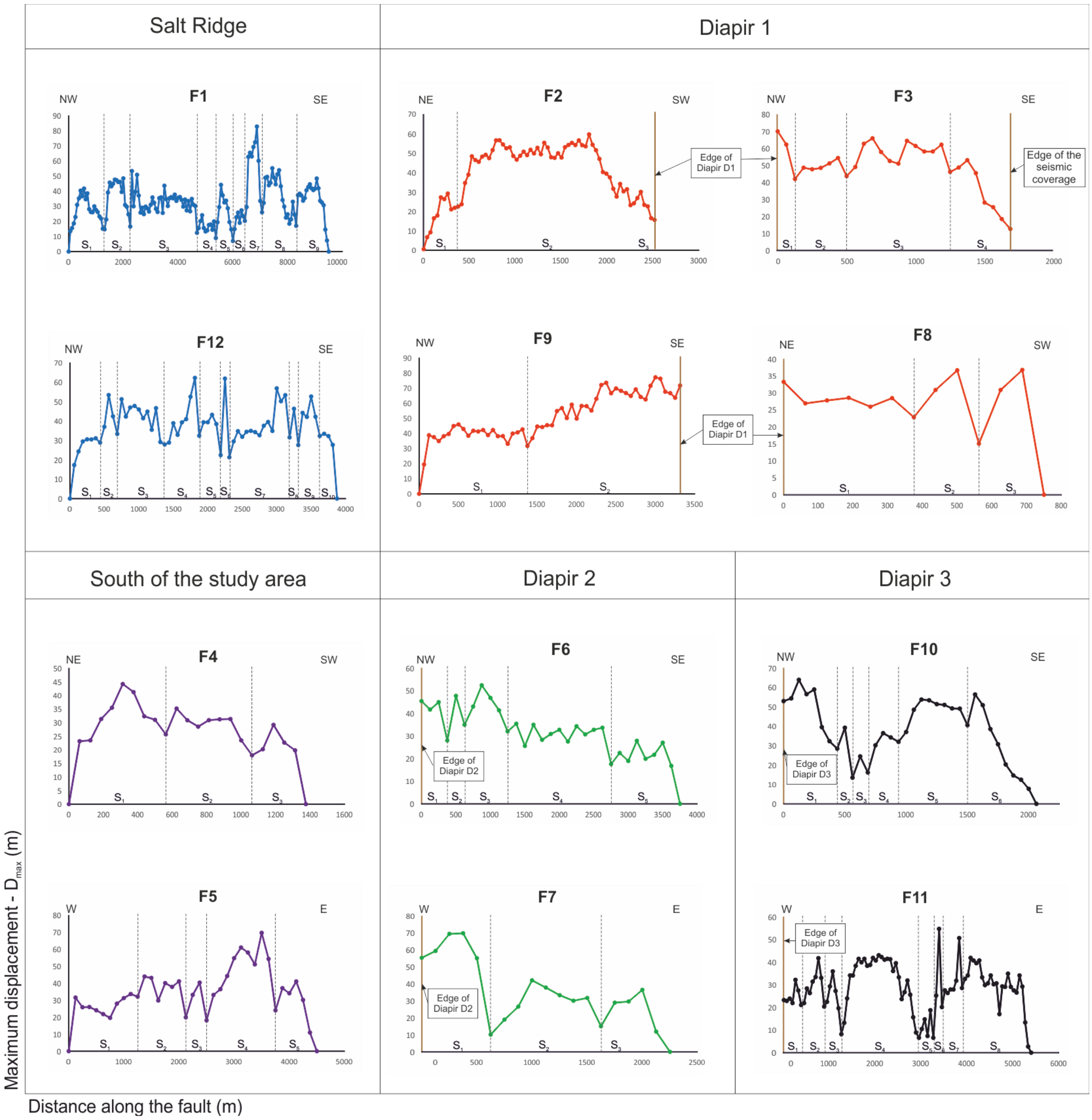

Figure 11: Displacement-length (D-x) plots for twelve representative faults. Faults are classified as C-type and M-type profiles based on Muraoka and Kamata (1983), as described in this work. Displacement curves were created along horizon H_5. Fault displacement and distance along the fault length are displayed in metres. Dotted lines and S1 to Sn denote distinct fault segments later linked to form a continuous fault plane.

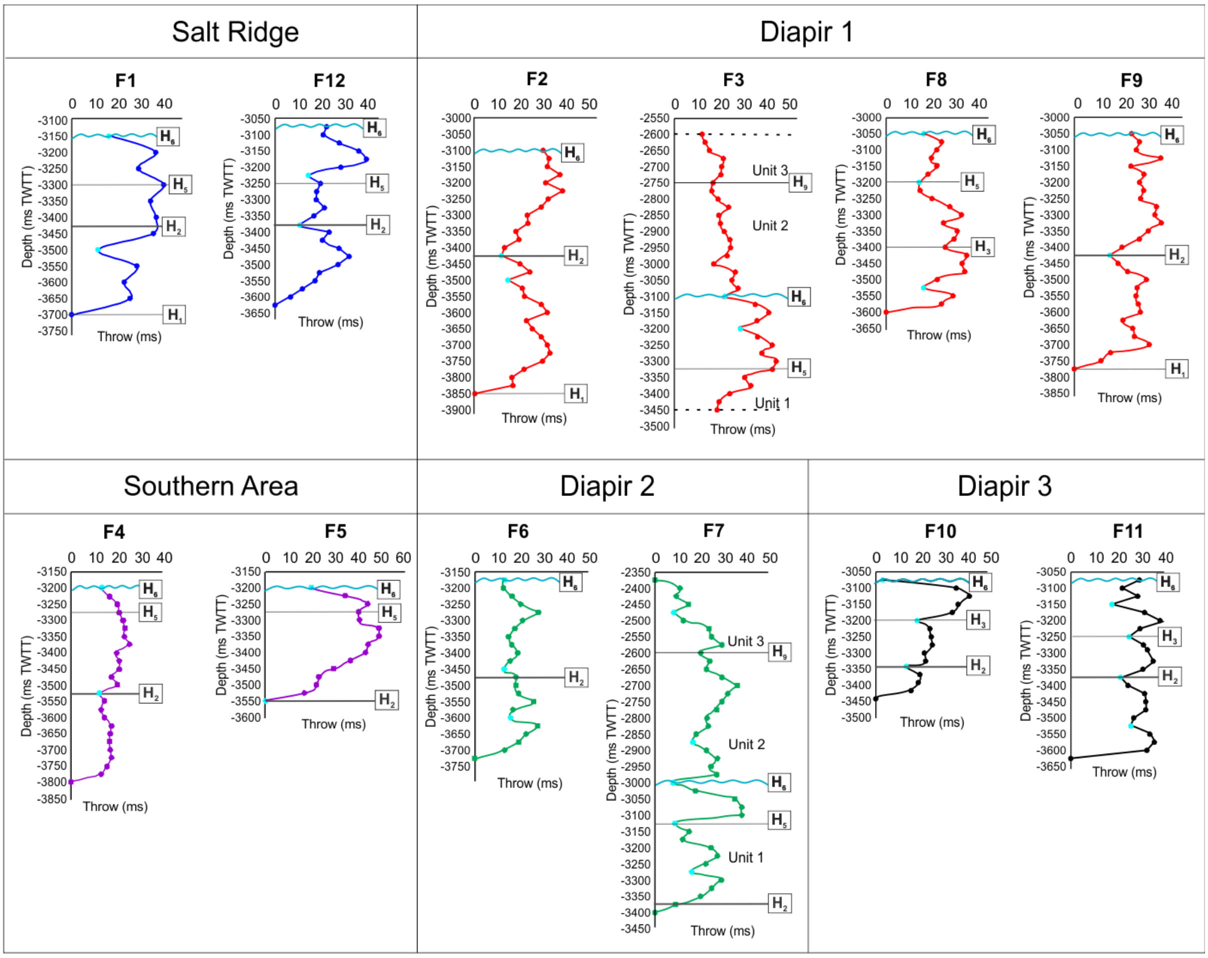

Figure 12: Throw-depth profiles for eight representative faults with both depth and throw measured in ms TWTT. Three throw profiles were identified based on these plots: asymmetric, M-type and skewed M-type. Grey lines indicate the horizons cut by the faults. The maximum throw for the majority of the faults occurs at horizon H_5. Throw minima are indicated by blue dots. The thick black line represents horizon H_2, where the first throw minima for most of the faults is recorded, whilst the blue line represents the Mid-Eocene unconformity (horizon H_6).

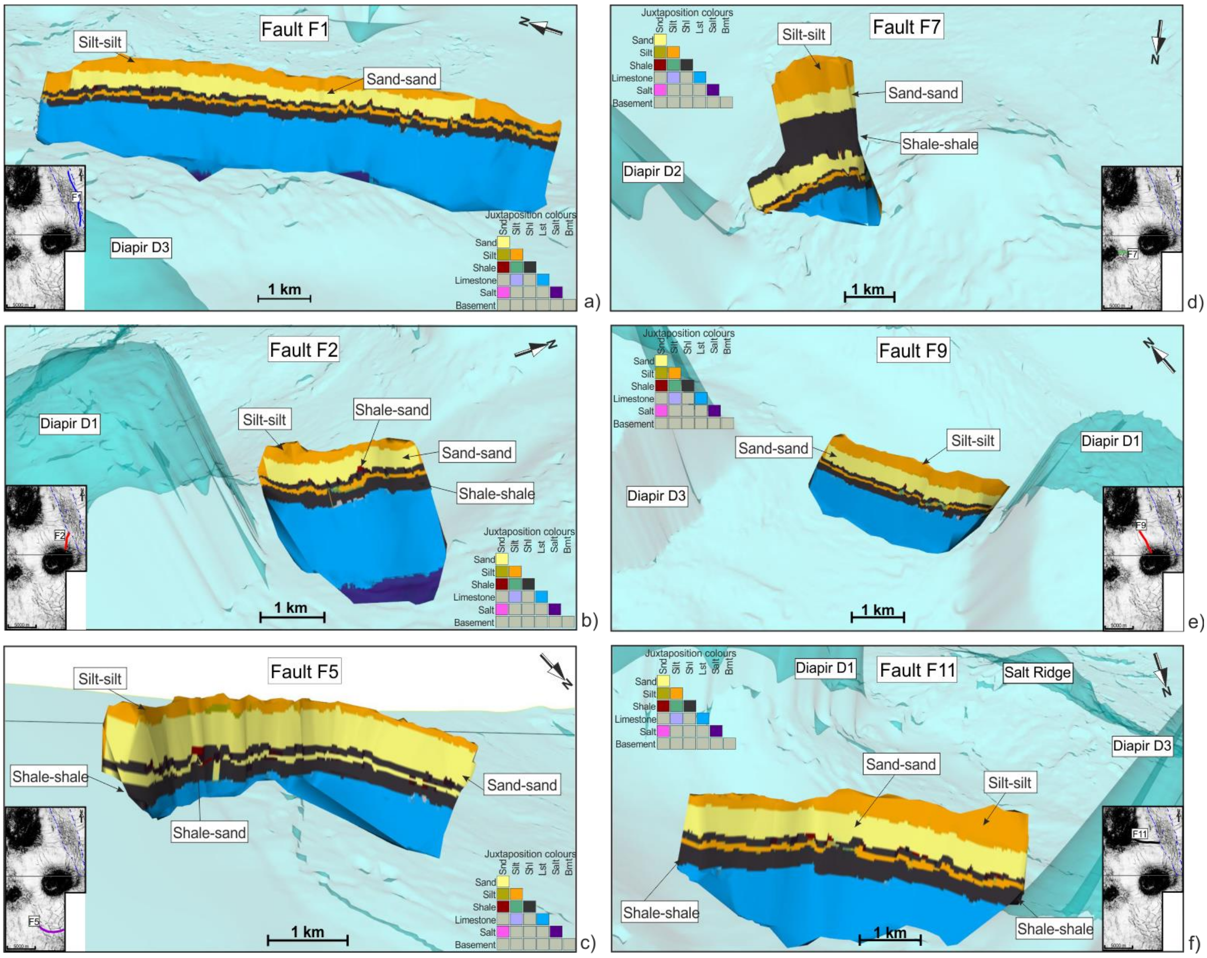

Figure 13: Juxtaposition diagrams for representative faults in the study area. a) Fault F1 showing juxtaposed sand units in its central part and a permeable interval defined by a shale interval. Close to the fault terminations juxtaposed limestone and sand-shale and sand-silt contacts are observed. b) Fault F2 showing sand units delimited vertically and laterally by impermeable units. c) Juxtaposition diagram for fault F5 showing an upper sand body laterally delimited by contacting silt units to W. d) Fault F7, showing that juxtaposed sand bodies are delimited vertically by a thin shale layer close to Diapir D2 e) Fault F9 showing a sand body isolated by a sit-silt juxtaposition at the NW and SE terminations. f) Fault 11 showing the sand-sand contact delimited vertically by a silt-silt juxtaposition that increases in thickness towards the Diapir D3. The diagrams use a colour code chart to indicate the degree of juxtaposition between distinct units. Superimposed shale units are indicated in brown along the fault trace, whereas sand juxtaposition is defined in yellow.

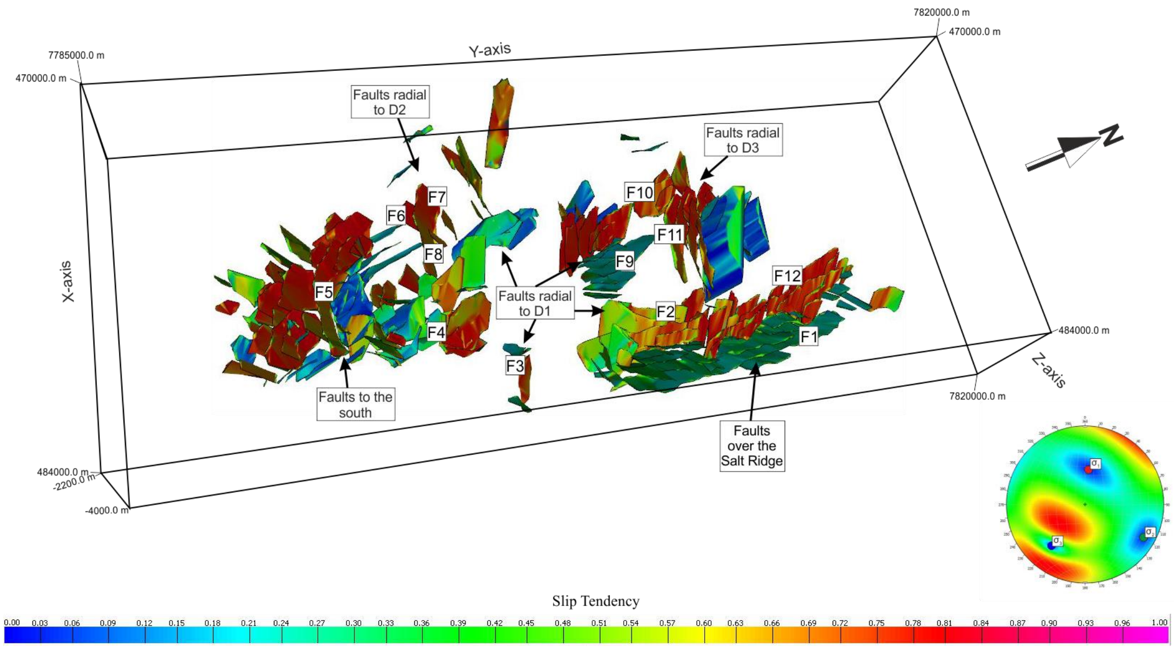

Figure 14: Slip tendency model for faults in the study area considering the paleostress tensor for the faults over the Salt Ridge. Slip tendency values range from 0.03 to 0.82, with an average of 0.53. Faults striking to NW show larger slip tendency values than faults striking to NE.

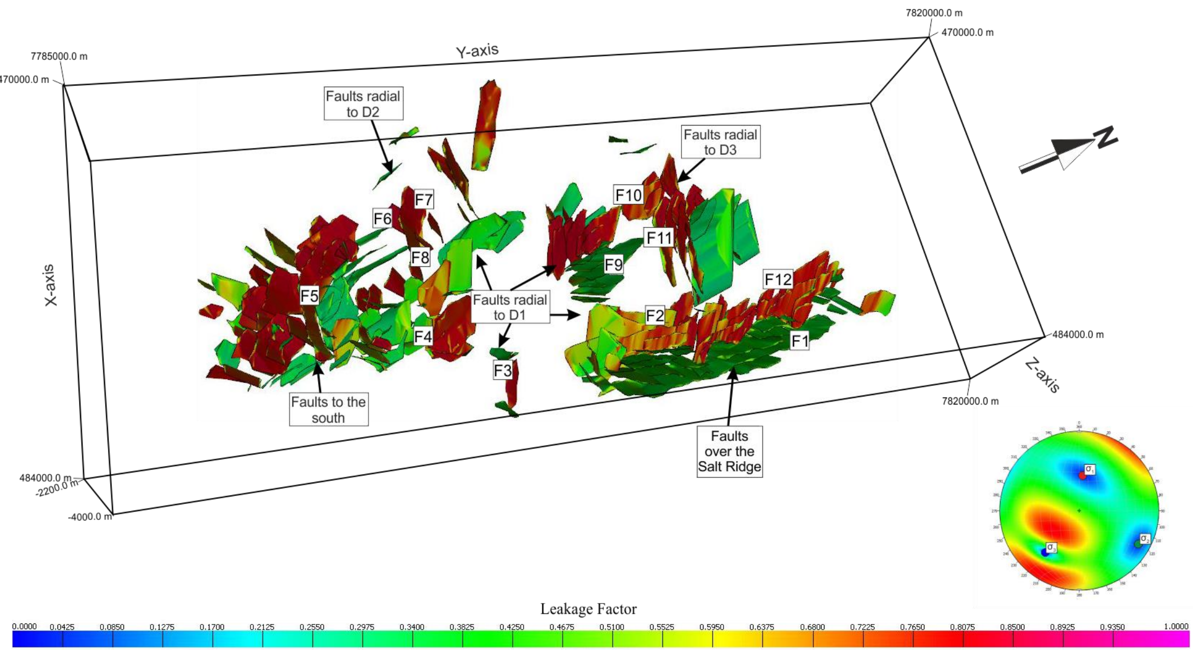

Figure 15: Leakage Factor model for faults in the study area considering the paleostress tensor for the faults over the Salt Ridge and a fluid pressure of 9 MPa. Leakage factors for the study area range from 0.27 to 0.85.

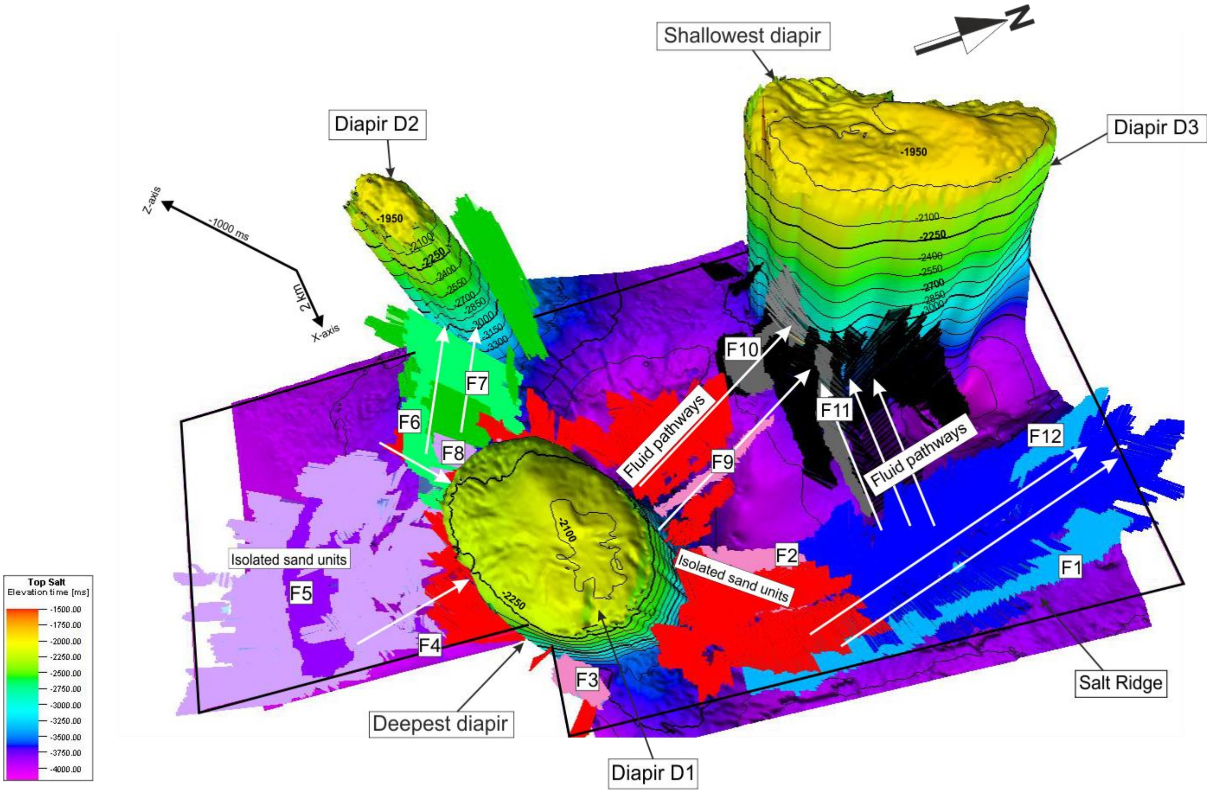

Figure 16: 3D representation of faults associated with halokinesis in the study area. The white arrows indicate a preferential fluid flow direction based on the leakage factor and juxtaposition analysis from south to north-northwest, in direction to D3. Isolated sand units were found in the vicinity of fault F2, adjacent to D1, and fault F5, in the southern part of the study area.